

POLITECNICO DI TORINO

MASTER OF SCIENCE IN ELECTRICAL ENGINEERING

A.Y. 2022/2023

**Control of a Microgrid based on
Virtual Synchronous Machine
Technology**



**Politecnico
di Torino**

Supervisors

Dr. Fabio MANDRILE
Vincenzo MALLEMACI

Candidate

Federico CAMPANELLI

October 6, 2023

*Whatever is begotten, born, and dies.
Caught in that sensual music all neglect
Monuments of unageing intellect.*

-W.B. Yeats

Acknowledgments

Let me start this thesis by thanking those who made it possible. Thanks to Fabio for being such a wise and kind mentor. Thanks to Vincenzo for sharing his deep knowledge about the field. Together they guided me and helped me achieve an otherwise unattainable goal.

I want to also thank everyone at PEIC for being such great role models and companions during my time there.

Moving on to my family I want to express my gratitude to my mom Elettra; who, alongside my grandmother Adele, has shown the ways of a fruitful academic career. Thanks to my brother Pietro for having shared his elder experience with me and thanks to my sister Ginevra for being a playfellow during my times at home. Thanks to my dad Filippo for his patience and support.

To my friends met at Politecnico I owe the great times I had there, in hindsight the best in my life. I feel in debt with you: Andrea, Marino, Pietro and all the others who have shared their path with me.

Contents

1	Abstract	1
2	Introduction	1
2.1	The Changing Paradigm	2
2.2	Distributed Generation	4
2.3	Microgrids	4
3	Grid Services	6
3.1	System Quality Objectives	6
3.2	Transmission Equations	9
3.2.1	Active and Reactive Power Decoupling on Lossless Lines	10
3.3	Frequency Regulation	11
3.3.1	ROCOF	13
3.3.2	Primary Regulation	15
3.3.3	Secondary Regulation	16
3.3.4	Power Distribution Among Generators	18
3.4	Static Voltage Regulation	18
3.5	Dynamic Voltage Regulation	20
4	Real and Virtual Synchronous Machines	21
4.1	Virtual Synchronous Machine	24
4.2	S-VSC	25
4.2.1	Power Conversion	27
4.2.2	Mechanical Emulation	28
4.2.3	Machine Equations	28
4.2.4	Excitation Control	29
4.3	Electromechanical Damping	30
5	Laboratory Setup	33
5.1	Grid interfaced Three phase Inverter	34
5.1.1	R1 Inverter	34
5.1.2	G1 & G2 Inverters	35
5.2	Grid Emulator and Microgrid Transformer	35
6	Personal Contributions to the Laboratory Setup	36
6.1	G1 & G2 Inverter Refurbishment	36
6.2	Grid Emulator Control	38
6.2.1	Dynamic Frequency Regulation	39
6.3	Rack Current Conditioning Board	40
6.4	Microgrid	41
7	Experimental Results	44
7.1	Single Inverter with Variable Grid	44
7.2	Two Inverters with Variable Grid	48
7.3	Three Inverters with Variable Grid	52

7.4	Three Inverters with Variable Stiff Grid	53
8	Islanding	57
9	Conclusions	59
9.1	Future Works	60

1 Abstract

The stability of the grid has been so far guaranteed by traditional Synchronous Generators (SGs) of thermo-electric power plants. SGs are being phased out in place of renewable energy sources interfaced to the grid through static converters. However, traditional inverter controls could not provide SG stability services. Therefore, new control algorithms based on the concept of Virtual Synchronous Machines (VSMs) have been proposed to make converters able to mimic traditional SGs. This thesis focuses on the implementation of a VSM solution called Simplified Virtual Synchronous Machine (S-VSM). In particular, the thesis provides simulations and experimental tests on a 45 kVA microgrid setup to analyze the real world response of the control strategies. The VSM will also be compared to traditional grid interfaced inverter controls to highlight the differences and improvements of the new generation of grid-tied inverters in providing stability to the grid. Finally, the tests will evaluate the capabilities of the S-VSM to operate in islanding mode and its stability during the transition.

2 Introduction

Modern power systems have been designed to obtain energy from primary sources: hydro, gas, coal and nuclear; transform it through the use of Synchronous Generators (SGs) and deliver it to the customers through AC lines. Thanks to climate driven choices and improvements in technology, energy generation has shifted towards Renewable Energy Sources (RES) [1]; these sources are often interfaced to the grid through a grid tied inverter.

Fig. 1 shows the trend of generation types and the roadmap towards a more sustainable future, following the European Commission Green Deal whose objectives are a 55% emission reduction with respect to 1990 within 2030 and a net zero continent by 2050.

Moreover the generation of power, while still mainly carried out by large power plants, is starting to become more distributed through the diffusion of prosumer communities: communities or neighborhoods where generation and demand are met locally thanks to the diffusion of microturbines, rooftop photovoltaic panels and small scale wind turbines. The decreasing number of SGs, i.e., the machines that have so far taken care of the system stability, and the advent of small producers that have limited participation in the control of the grid can lead to an unstable system if the former role of SGs isn't taken by other players, i.e., RES interfaced to the grid through static converters. [2].

This is why there's been a wide research on Virtual Synchronous Machines (VSM) [3, 4], algorithms that make grid-tied converters able to mimic the behavior of SGs through an equivalent mathematical modeling of it and provide the system with inertia, voltage and frequency control and harmonic mitigation.

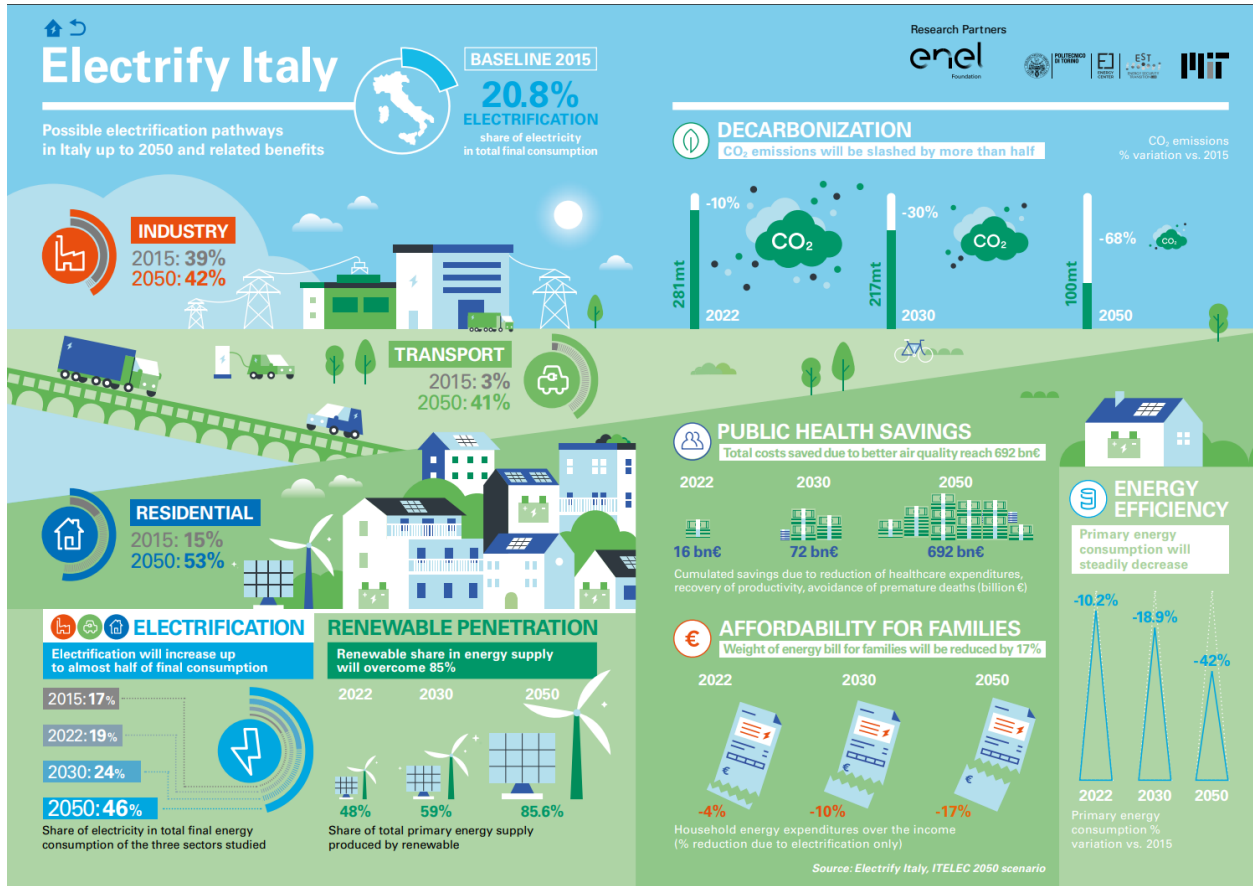


Figure 1: Electrify Italy Report [5].

e-Mobility and prosumers generate a higher than ever power demands but also constitute a resource thanks to vehicle to grid (V2G) technologies and microgrids. Microgrids indicate self sufficient portions of the network that can either work independently or tied to the main distribution system. The advantages are a higher reliability of generation and distribution and the possibility of exploiting combined production [6] of resources thus decreasing the cost of operation.

2.1 The Changing Paradigm

The ELIT study [5] carried out jointly by Politecnico di Torino, Massachusetts Institute of Technology and Enel highlights how the current energy paradigm is not sustainable in the long term, causing the need of a new paradigm. Such paradigm needs to be centered on the so called energy trilemma:



This is a recollection of the main goals needed for a system disjointed from finite resources. *Sustainability* means that no long term effects arise from the system; both environmental and ecological. This is opposed by the current paradigm of polluting fossil fuels and their limited supply. At the current rate of consumption the forecasts in supply duration are very limited. Studies by BP Statistical Review of World Energy 2021 indicate proven reserves to last less than 50 years for natural gas, 50 years for oil and 130 years for coal. With the current increase in consumption trends the real figures might be even lower. The need for a more sustainable grid is then apparent. What is more, CO_2 levels are increasing due to fossil fuel emissions as recorded by NOAA Mauna Loa Observatory, the mean surface and air temperature are increasing because of greenhouse effects and the sea level are rising due to ice cap melting as shown in Fig. 2 [7].

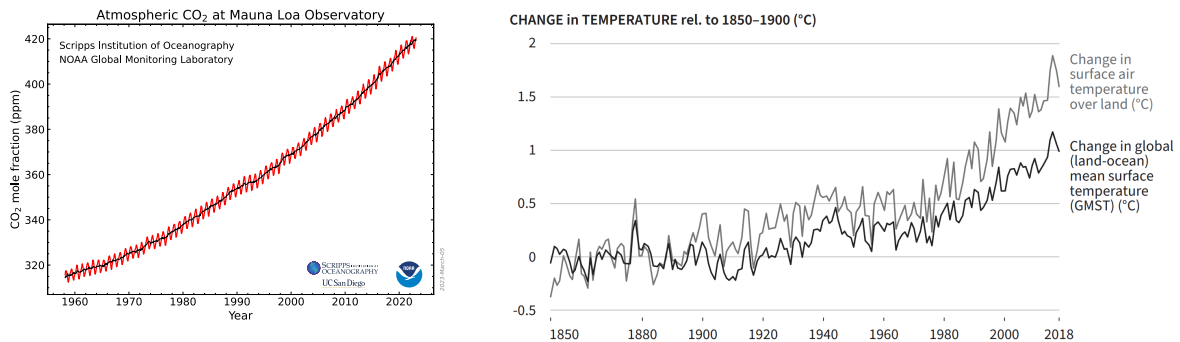


Figure 2: CO_2 levels and earth temperature recording.

Security indicates a geopolitical and technical matter. Energy delivery to a country must be secure in the short and long term. This translates in a reliable grid and a reliable grid and independence from autocracies and dictatorships. The current crisis due to the Russian invasion of Ukraine has highlighted the importance of this. In a speech following the invasion the Italian P.M. Mario Draghi pronounced: "As had observed the historian Robert Kagan, the jungle of history has returned, and its vines want to wrap around the garden of peace in which we thought to live in". This political event has also shifted security from the least to the most important point of the energy trilemma. It is through local, renewable and independent energy sources that it is possible to achieve energy this trilemma point.

Equity is the ability of a system to provide reliable and affordable energy for everybody.

This means decoupling the price of energy from the gas and oil market, a market heavily invested in geopolitics and speculation. RES can allow – with a proper infrastructure – a more stable price of electricity and microgrids can allow remote and isolated areas to have access to this commodity.

2.2 Distributed Generation

The current centralized paradigm of energy generation – carried out in powerplants and distributed to the final users through a meshed High Voltage (HV) infrastructure – can be seen to evolve into a distributed generation paradigm, depicted in Fig. 3 [1].

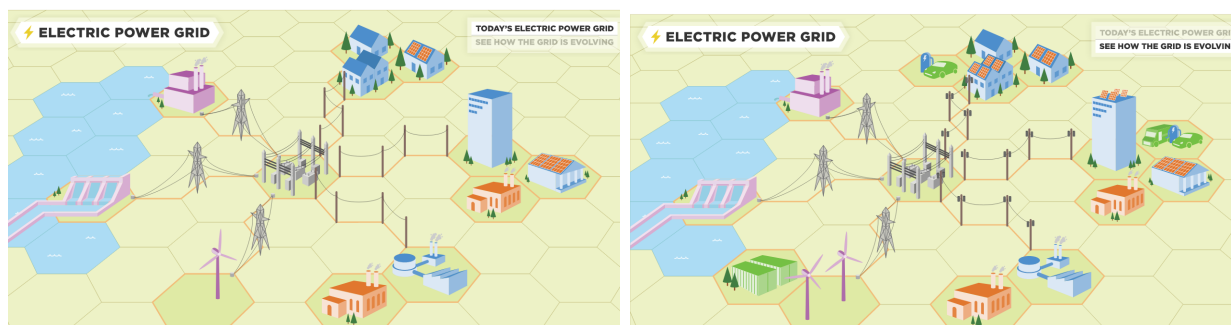


Figure 3: From Centralized to Distributed Generation. Source: epa.gov.

The goal of a distributed generation and more broadly of a Smart Grid is interfacing the Intelligent Electronic Devices (IEDs) like smart meters, voltage and current sensors and Phasor Measurement Units (PMUs) to a control system called Supervisory Control and Data Acquisition (SCADA) to supervise and optimize the Distribution System (DS). This system, through state estimations, displays to the Transmission System Operator (TSO) the real time conditions of the Distribution Network (DN) and allows it to control voltage profiles among lines, to optimize local power generation and consumption by varying the setpoints of Distributed Energy Resources (DER) and providing, through the use of smart substations, automatic breaker and sectioner re-closures in case of branch faults. Operation which would have taken much longer through the employment of technicians. This has the goal of minimizing yearly off-line periods of customers to achieve the national standards.

2.3 Microgrids

Microgrids increase the availability of DER, which are frequently renewable – namely rooftop solar Photovoltaic (PV) panels – and allow the use of cogeneration. This increases synergy and optimization of the total energy consumption of buildings and industries. Moreover, they provide resilience to contingencies as during external faults they can provide energy to the local system as they can provide energy to the local system during external faults and they can draw energy from the Distribution Grid (DG) during internal faults.

In Fig. 4 there is a representation of a microgrid layout. As it is shown, the DG is interfaced with a breaker, meaning that the connection is controlled by the microgrid control system. A battery storage or controlled sources like Fuel-cells and Hydrogen turbines are

necessary because, as explained in chapter 3.3, the load power and the input power must always coincide and this is not always possible with just RES because of their intermittent power generation.

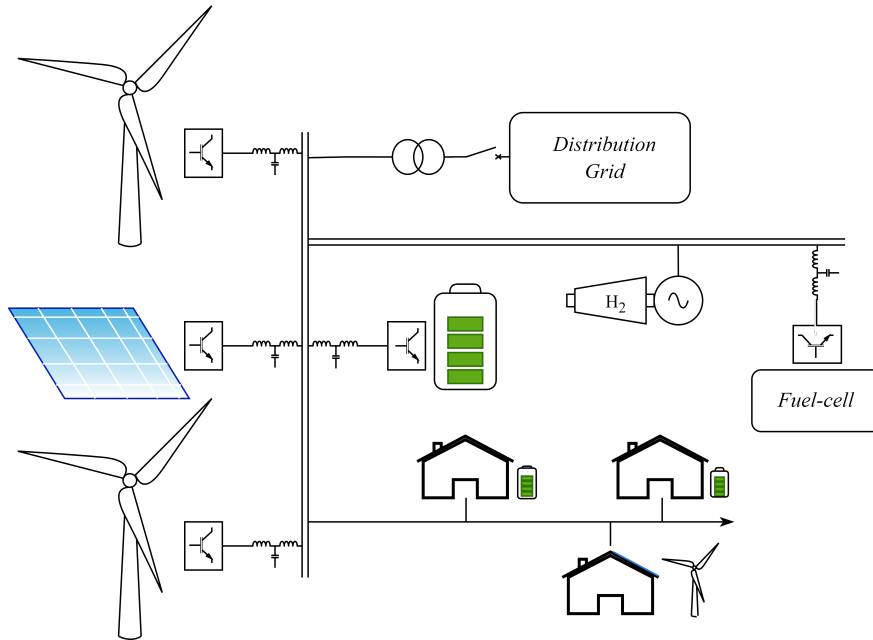


Figure 4: Microgrid layout.

3 Grid Services

Power systems, exemplified in Fig. 5 as we know them have as services:

- Active power delivery and frequency control;
- Reactive power delivery and voltage control;
- Active and reactive power reserves;
- Short circuit power.

Historically, the main goal of a dist system is to deliver active power from the generators to the users. The system operates by imposing a voltage at a specific frequency. As we will see, the frequency of such system must comply with strict requirements managed by the TSO.

Reactive power can flow in either directions and it is an artifact of the Alternated Current system. This power has to be taken care of either by generators, Power Factor Correctors (PFCs) or grid tied inverters. Associated to reactive power is the voltage amplitude.

Active power production is scheduled day by day through load curve forecasting and the power-plants bid to acquire share of the power needed to be produced. Reserves are there to account for miscalculations in forecasting and unforeseen events Nowadays they also take into account the unforeseeable behavior of RES.

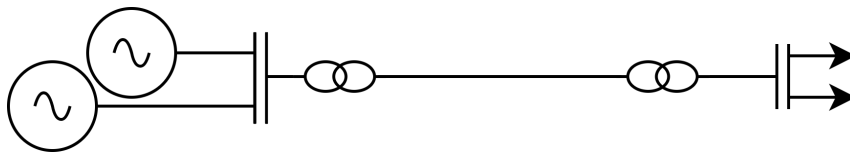


Figure 5: Basic schematic of a distribution system.

The last grid service – short circuit power – indicates the fault current of a power system. This is needed to activate the protection equipment and be sufficiently high to not be mistaken for a normal operation current.

3.1 System Quality Objectives

The Distribution System has to guarantee operation within certain limits imposed by the European Commission and ENTSO-E which are then deliberated by the national TSOs.

Norms and regulations of particular interest to this thesis are:

- Commission Regulation (EU) 2017/1485 of 2 August 2017: Establishing a guideline on electricity transmission system operation [8];
- Deliberation 84/2012: Urgent actions related to electricity production systems, with particular reference to the distributed generation, to guarantee the security of the national electrical system [9];
- CEI 0-21 (Low Voltage Fault Ride Through capability);

- CEI 0-16 (Converter Interfaced Medium Voltage Fault Ride Through capability).

In particular, the Commission Regulation imposes the steady state and transient objectives for voltage and frequency, summarized in the Annex II and III:

Table 1

Voltage ranges at the connection point between 110 kV and 300 kV

Synchronous area	Voltage range
Continental Europe	0,90 pu-1,118 pu
Nordic	0,90 pu-1,05 pu
Great Britain	0,90 pu-1,10 pu
Ireland and Northern Ireland	0,90 pu-1,118 pu
Baltic	0,90 pu-1,118 pu

Figure 6: Annex II from Commission Regulation [8].

Table 1

Frequency quality defining parameters of the synchronous areas

	CE	GB	IE/NI	Nordic
standard frequency range	± 50 mHz	± 200 mHz	± 200 mHz	± 100 mHz
maximum instantaneous frequency deviation	800 mHz	800 mHz	1 000 mHz	1 000 mHz
maximum steady-state frequency deviation	200 mHz	500 mHz	500 mHz	500 mHz

Figure 7: Annex III from Commission Regulation [8].

These values state the quality objectives of the European grid, which are then adjusted to the particular case operation. As for voltage related aspects the norms CEI 0-16 and 0-21 state that for low and medium voltage applications the converter has to remain connected under any circumstances within voltage ranging in:

$$0.85 < V < 1.15 \quad [pu]$$

This trend refers to the steady state operation of the converter. Moreover, Fault Ride Through (FRT) curves – reported in Fig. 8 – define the dynamic behavior of the Voltage-time trend under which the converter must still be connected:

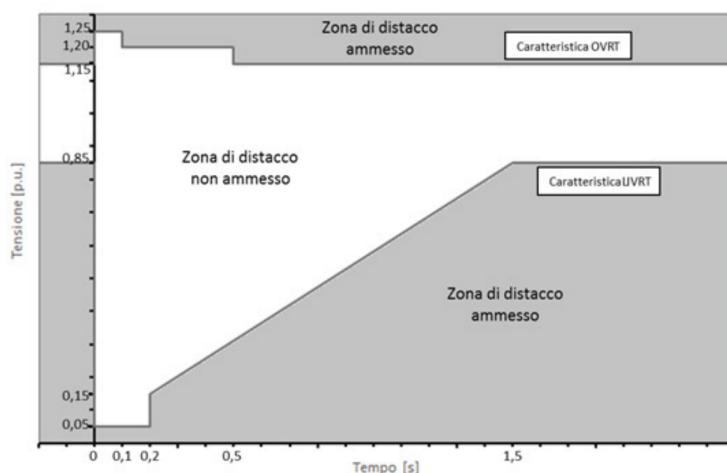


Figure 8: Fault Ride Through curves for low and medium voltage static converters [10].

Historically, RES inverters were programmed to disconnect for frequency deviations above 0.3 Hz , as the share of renewable production increased, the limit raised concerns for the stability and security of the system. Line tripping, generation loss or abrupt load increase cause a frequency drop of the entire system. This is then compensated by frequency regulation as explained in chapter 3.3. In a letter of 2012, the ENTSO-E president communicated [9] the new frequency cutoffs are:

$$47.5 < f < 51.5 \text{ [Hz]}$$

This update – which corresponds to conventional generators cutoff – had the goal to increase the system stability.

Analogous to the voltage FRT curve, there exists a frequency capability curve that is mandated by ENTSO-E and rectified by national TSOs, an example of which is shown in Fig 9.

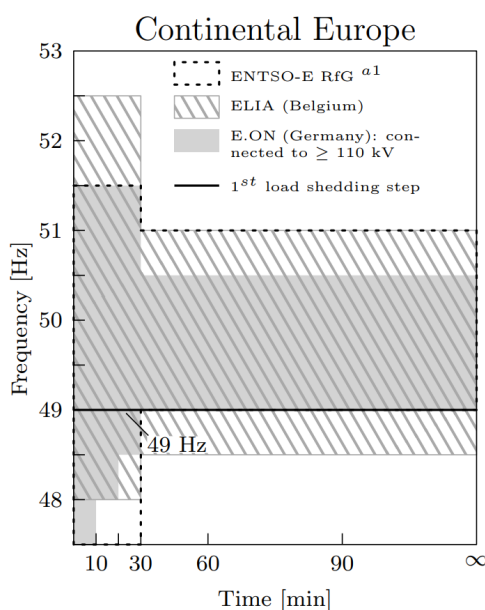


Figure 9: ENTSO-E frequency capability curves for continental Europe [11].

3.2 Transmission Equations

Modeling an AC line between a Sending (S) and Receiving (R) end using the sign convention of Fig. 10 [12]

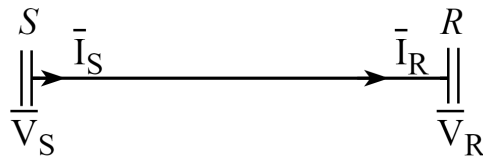


Figure 10: Sign convention for transmission line analysis.

we can obtain the bipole transmission matrix; this matrix is fundamental for modeling any AC system and is crucial for our study:

$$\begin{bmatrix} \bar{V}_S \\ \bar{I}_S \end{bmatrix} = \begin{bmatrix} \cosh(\bar{\gamma}a) & \bar{Z}_0 \cdot \sinh(\bar{\gamma}a) \\ 1/\bar{Z}_0 \cdot \sinh(\bar{\gamma}a) & \cosh(\bar{\gamma}a) \end{bmatrix} \begin{bmatrix} \bar{V}_R \\ \bar{I}_R \end{bmatrix} \quad (1)$$

Where a is the length of the line, γ is the propagation constant and \bar{Z}_0 is the characteristic impedance:

$$\bar{\gamma} = \sqrt{(r + j\omega l)(g + j\omega c)} \quad (2)$$

$$\bar{Z}_0 = \sqrt{\frac{(r + j\omega l)}{(g + j\omega c)}} \quad (3)$$

Where, r , l , g , c represent the unit length parameters of resistance, inductance, conductance and capacitance for a transmission line. For an analytical simplification the high and medium voltage lines are studied under lossless hypothesis, this implies ($r = g = 0$). The typical inductance and capacitance – which are mainly a function of the number of cables (n) – of a line are:

n	V_n	$x = \omega l$ [Ω/km]	c [nF/km]
1	(LV), MV, HV	≈ 0.4	≈ 9
2	HV (< 220 kV)	≈ 0.3	≈ 12
3	HV (> 220 kV)	≈ 0.25	≈ 13

Table 1: UNIT LENGTH PARAMETERS OF A TYPICAL AERIAL TRANSMISSION LINE.

It is interesting to note that the propagation speed of the voltage and current – under the lossless hypothesis – is equal to: $v_p = 1/\sqrt{lc}$; under these hypothesis the equations get simplified to:

$$\bar{\gamma} = j\omega\sqrt{lc} \quad (4)$$

$$\bar{Z}_0 = \sqrt{\frac{l}{c}} = Z_0 \quad (5)$$

Moreover the term of the hyperbolic argument $\bar{\gamma}a = j\omega\sqrt{lc}a = j\theta$ where θ is a real angle which is a function of the length of the line and its parameters. The hyperbolic functions with argument $j\theta$ are simplified to:

$$\cosh(j\theta) = \cos(\theta), \quad \sinh(j\theta) = j \cdot \sin(\theta)$$

The transmission matrix under lossless hypothesis is then rewritten as:

$$\begin{bmatrix} \bar{V}_S \\ \bar{I}_S \end{bmatrix} = \begin{bmatrix} \cos(\theta) & jZ_0 \cdot \sin(\theta) \\ j/Z_0 \cdot \sin(\theta) & \cos(\theta) \end{bmatrix} \begin{bmatrix} \bar{V}_R \\ \bar{I}_R \end{bmatrix} \quad (6)$$

3.2.1 Active and Reactive Power Decoupling on Lossless Lines

By using the receiving end voltage as reference for the phase angle ($\bar{V}_R = V_R e^{j0}$) and deriving the source voltage expressed as $\bar{V}_S = V_S e^{j\delta}$:

$$\bar{V}_S = V_S e^{j\delta} = V_S \cos(\delta) + jV_S \sin(\delta) = V_R \cos(\theta) + jZ_0 \bar{I}_R \cdot \sin(\theta) \quad (7)$$

$$\bar{I}_R = \frac{V_S \cos(\delta) + jV_S \sin(\delta) - V_R \cos(\theta)}{jZ_0 \cdot \sin(\theta)} \quad (8)$$

Calculating the power at the receiving node:

$$S_R = P_R + jQ_R = \bar{V}_R \cdot \bar{I}_R^* \quad (9)$$

By using equations (8) and (9) we can obtain:

$$P_R = \frac{V_S V_R}{Z_0 \sin(\theta)} \sin(\delta) \quad (10)$$

$$Q_R = \frac{V_R}{Z_0 \sin(\theta)} (V_S \cos(\delta) - V_R \cos(\theta)) \quad (11)$$

Exploiting the symmetry of the system we can, by applying some transformations, derive the equations for the receiving end by:

- Inverting S and R pedices
- Inverting the phase shift sign
- Inverting the power signs

$$-P_S = \frac{V_S V_R}{Z_0 \sin(\theta)} \sin(-\delta) \quad (12)$$

$$-Q_S = \frac{V_S}{Z_0 \sin(\theta)} (V_R \cos(-\delta) - V_S \cos(\theta)) \quad (13)$$

And finally

$$P_S = \frac{V_S V_R}{Z_0 \sin(\theta)} \sin(\delta) = P_R \quad (14)$$

$$Q_S = \frac{V_S}{Z_0 \sin(\theta)} (V_S \cos(\theta) - V_R \cos(\delta)) \quad (15)$$

Under the hypothesis of small phase shift $\cos(\delta) \simeq 1$ and a prevalent inductive line $\cos(\theta) = \cos(\omega\sqrt{lc}) \simeq 1$ – as is proper in most transmission lines and cables – we can derive

$$\lim_{c \rightarrow 0} Z_0 \sin(\theta) = \sqrt{\frac{l}{c}} \sin(\omega\sqrt{lc}a) = \omega la = xa = X \quad (16)$$

This means that transmission lines, transformers and cables can be represented by a longitudinal reactance.

Therefore it is possible to rewrite the equations:

$$P_S = P_R = \frac{V_S V_R}{X} \sin(\delta) \quad (17)$$

$$Q_R = \frac{V_R}{X} \cdot \Delta V \quad (18)$$

$$Q_S = \frac{V_S}{X} \cdot \Delta V \quad (19)$$

The reactive power absorbed by the line Q_{ab} is therefore proportional to:

$$Q_{ab} = Q_S - Q_R = \frac{V_S - V_R}{X} \cdot \Delta V = \frac{\Delta V^2}{X} \quad (20)$$

From (17, 18, 19) it is possible to conclude that the voltage V – in a mostly inductive line – is proportional to the reactive power while the phase shift δ is proportional to the active power.

3.3 Frequency Regulation

Frequency regulation is a necessary regulation to keep the power system stable. The frequency of continental Europe is set at 50 Hz, under normal operating conditions the system is isofrequential and the central monitoring of the frequency is done by SwissGrid. The maximum allowable delay from synchronization is 30 s, after which corrective maneuvers are done to re-synchronize the system – namely increasing the frequency setpoint by 15 mHz.

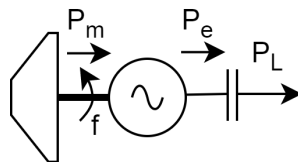


Figure 11: Equivalent diagram of the swing equation.

At the core of frequency regulation resides the swing equation, this is obtained supposing a 2 poles machine (thus obtaining that the mechanical frequency coincides with the electrical one).

We can define the parameters of the swing equation in Table 2:

P_m	Mechanical power
P_e	Electrical power
P_L	Electrical load
f	frequency
J	Moment of Inertia

Table 2: PARAMETERS OF THE SWING EQUATION.

From the mechanical equation of a generator we know that:

$$J \frac{d\omega}{dt} = T_m - T_e \quad (21)$$

Under the hypothesis of almost constant frequency we can say that $P_x = T_x \cdot \omega_n$ where ω_n is the nominal grid pulsation. We can thus write:

$$\frac{J \cdot \omega_n^2}{S_n} \cdot \frac{d}{dt} \left(\frac{\omega}{\omega_n} \right) = \frac{P_m - P_e}{S_n} \quad (22)$$

After having defined $T_a = J \cdot \omega_n^2 / S_n$, $\omega_{pu} = \omega / \omega_n$ and $P_x^{pu} = P_x / S_n$; we can obtain the following:

$$T_a \frac{d\omega_n}{dt} = P_m^{pu} - P_e^{pu} \quad (23)$$

Where T_a is dimensionally a time [s], this can be interpreted as the time needed to reach the nominal velocity through a constant input torque. Its order of magnitude is $T_a \approx 6 \div 12$ s. International literature though uses the inertia constant defined as $H \equiv T_a / 2$, typical values of it are shown in Fig. 12.

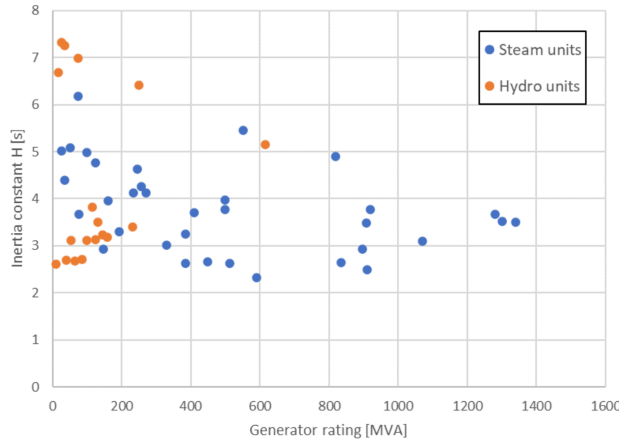


Figure 12: Time constants for various generation plants. [13]

Conveniently the equation can also be re-written – by defining $M \equiv T_a \cdot S_n / f_n$ – as:

$$M \frac{df}{dt} = P_m - P_e \quad (24)$$

The term $M \frac{df}{dt}$, which represents the inertial term, is also often re-written as $P_W = -M \frac{df}{dt}$; thus obtaining:

$$P_e = P_W + P_m \quad (25)$$

The equation can also be linearized:

$$M \frac{d\Delta f}{dt} = \Delta P_m - \Delta P_e \quad (26)$$

During steady state operation (i.e., $\frac{df}{dt} = 0$) equation (24) tells us that the electrical power – i.e. the load of the line plus losses – must be equal to the mechanical input to the generators.

During transients we can conclude, thanks to equation (25), that the sum of mechanical input, electrical power and inertial power is always zero; this is related to Bucherot's law of powers. The frequency during faults follows a typical trend like represented in Fig. ?? and it is characterized by three phases: in the beginning the load is supplied by the inertial power characterized by the Rate of Change of Frequency (ROCOF) defined at $t \rightarrow 0^+$.

The second phase, called Primary Regulation, is carried out by a proportional control loop whose role is to limit the minimum frequency value (Nadir) and to restore the power balance between generation and consumption. The Secondary Regulation is achieved using an integral gain in the control loop and serves the purpose of eliminating the steady state error dictated by the proportional gain of the primary regulation.

The data to obtain this simulation are (their meaning will be explained in the following chapters):

$$\Delta P_L \quad 0.2pu \quad | \quad H \quad 3s \quad | \quad b_p \quad 5\% \quad | \quad T_s \quad 70s$$

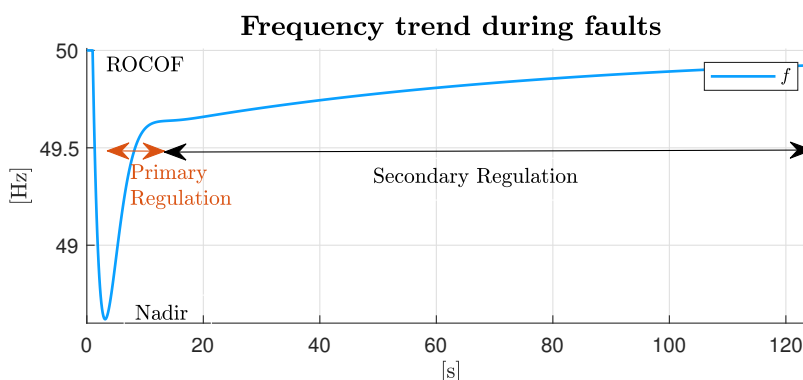


Figure 13: Frequency trend during faults.

3.3.1 ROCOF

The ROCOF is directly and solely related to the system inertia, or to the weighted average in a multi generation system as explained in chapter 3.3.4:

$$\frac{df}{dt} = -\frac{\Delta P_L}{M} \quad (27)$$

The system's inertia, defined by ENTSO-E [14] Total System Inertia (TSI), is crucial for a system and concerns are arising due to the foresee RES penetration in the share of production. And this leads – without countermeasures – to a decrease in TSI below the critical value of 2 s. In the past years, the decrease of TSI led to some incidents. For instance, in 2012 in GB [14] an incident of loss of generation due to a too high ROCOF forced the TSO to take costly measures at times of high RES production by shifting part of the load to SGs to increase the TSI. The costs sustained by Great Britain to avoid low TSI in 2013 show an increase from 60 M£ the previous year to 150 M£; and have been foreseen to billions of pounds in 2030.

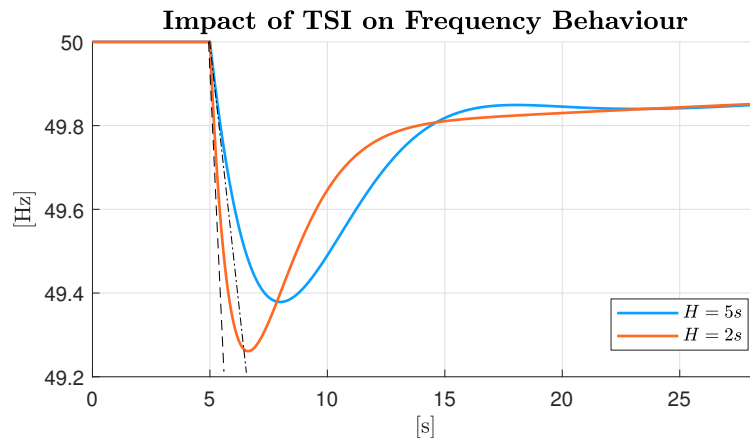


Figure 14: System frequency behavior with different TSI.

The dashed lines of Fig. 14 indicate qualitatively the initial slope of the frequency highlighting the difference between the two TSI. According to the Asset Study by the European Commission [13] and the national grid codes, the "Maximum ROCOF for which the Power Generating Module shall stay connected" per European country vary between 2 and 2.5 Hz/s, Italy being 2.5 Hz/s.

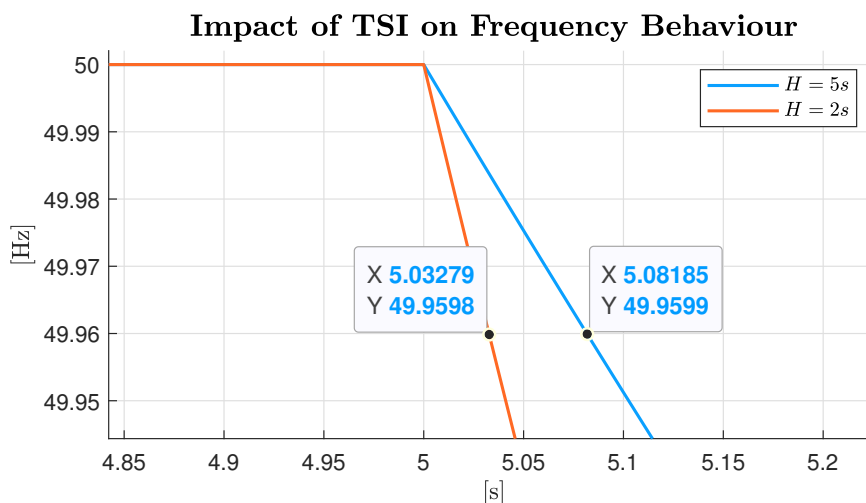


Figure 15: Zoomed detail of frequency ROCOF ($\Delta P_L = -0.1$).

Calculating the derivative of the frequency we obtain:

$$\Delta f_{H=5s}/\Delta t = 0.49 \text{ Hz/s}$$

$$\Delta f_{H=2s}/\Delta t = 1.23 \text{ Hz/s}$$

It coincides with the theoretical values $\Delta f/\Delta t = -\Delta P_L/(2 \cdot H)$ of 0.5 Hz/s and 1.25 Hz/s respectively.

Calculating the ROCOFs for typical ΔP_L [p.u.] and H constants yields the following Fig. 16.

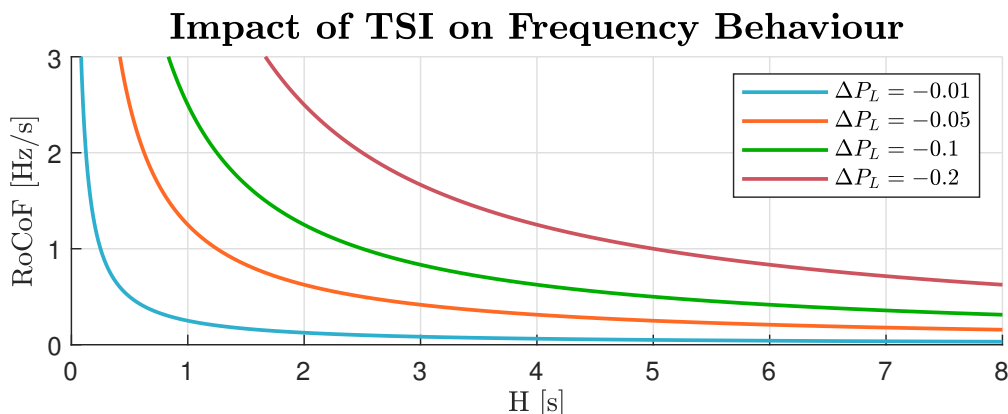


Figure 16: ROCOFs under various TSI.

3.3.2 Primary Regulation

To account for rotational loads the electrical power is defined as: $\Delta P_e = \Delta P_L + E_c \cdot \Delta f$. When the load changes the frequency starts dropping – or rising – because of the imbalance in the input and output power; the regulation then sees this imbalance and increases – or decreases – the power production of the system to reach the new equilibrium. Because the gain is purely proportional there will be an error at steady state. Participation to primary regulation is mandatory for generators with nominal power greater than 10 MW according to the Italian grid code annex A.15. Photovoltaic and Wind farms are – according to the annexes A.17 and A.68 – mandated to participate when connected to the HV distribution lines (> 110 kV) [10, 15]. The grid code annex A.15 also requires a "Primary Regulation Bandwidth" B_{pr} which must be 1.5% of the nominal power of the generator unit that participates to primary regulation. This means that under normal operating conditions only [1.5 - 98.5]% of the power available can be injected into the grid.

The control loop for primary regulation is the following:

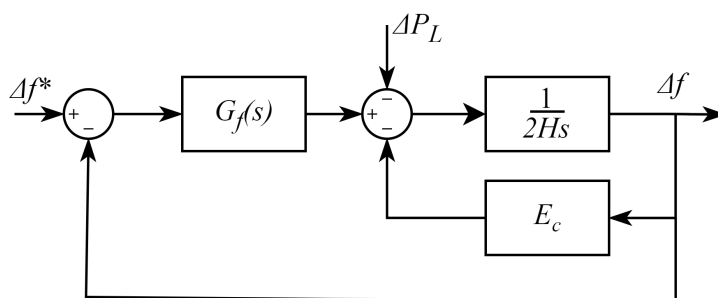


Figure 17: Primary regulation control loop.

The transfer function $\Delta f/\Delta P_L$ is:

$$\Delta f = -\frac{\Delta P_L}{2Hs + E_c + G_f(s)} \quad (28)$$

G_f is the transfer function of the plant and it has the following general expression:

$$G_f(s) = E_p \frac{1 + T_z s}{1 + T_p s} \quad (29)$$

This transfer function is proper of the steam turbines while it is artificially implemented in other kinds of generator to emulate the behavior. To find the steady state error it is necessary to impose $s = 0$, thus obtaining:

$$\Delta f = -\frac{\Delta P_L}{E_p + E_c} \quad (30)$$

The gain E_p is obtained through the selection of a *statism* value b_p . This is a percentage value used to size primary regulation; its value is typically 5% and the relation is:

$$b_p = \frac{P_n}{E_p \cdot f_n} \quad (31)$$

where P_n is the nominal value of the generator power and f_n is the nominal operating frequency – in all our cases 50 Hz.

For primary regulation the frequency set point is almost always 50 Hz, so Δf^* is usually neglected.

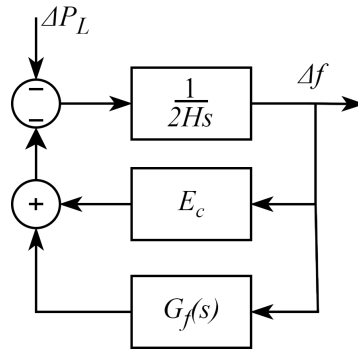


Figure 18: Primary regulation control loop with $\Delta f^* = 0$.

3.3.3 Secondary Regulation

Through an integral gain control loop the secondary regulation aims at restoring the steady state error, time constants of secondary regulations range from $T_s = 50 - 100$ s; this is done to avoid interaction between the two controls.

The loop control of secondary regulation is the following:

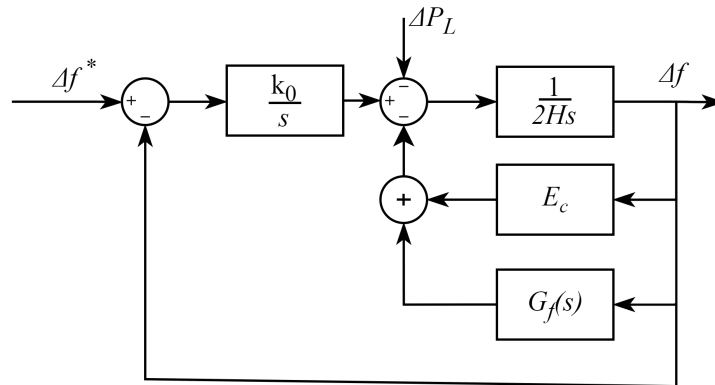


Figure 19: Secondary regulation control loop.

To set the gain of the secondary regulation we can approximate the primary regulation to its steady state gain $1/(E_p + E_c)$. By doing this we obtain the following:

$$\left(\frac{d\Delta f^*(s)}{d\Delta f} \right)_{\Delta P_L=0} = \frac{1}{1 + s \frac{E_p + E_c}{k_0}} \quad (32)$$

The time constant of the transfer function just found is:

$$T_s = \frac{E_p + E_c}{k_0} \quad (33)$$

In a multi-generator system, given the pole in the origin of the gain of secondary regulation and the inherent measurements error that would happen at each measuring point, the error is calculated at centralized level and sent to the generators participating to the secondary regulation (called conventionally y):

$$y = (\Delta f^* - \Delta f) \cdot \frac{k_0}{s} \quad (34)$$

Block diagram of centralized secondary regulation is depicted in Fig. 20.

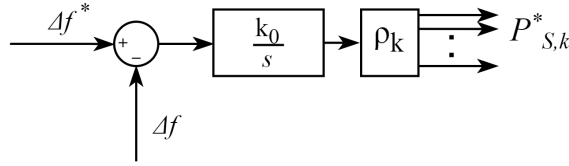


Figure 20: Block diagram of centralized secondary regulation.

Plants participating to Secondary Regulation must allocate a bandwidth $B_{sr}P_n$ – which is added to the Primary Regulation bandwidth – which is typically 6% for termoelectric plants and 15% for hydroelectric plants.

The total secondary regulation bandwidth is calculated by adding all the bandwidths of the individual generators participating to the secondary regulation:

$$R_S = \sum_N B_{srk} \cdot P_{nk} \quad (35)$$

In Italy the secondary regulation bandwidth is equal to ≈ 600 MW.

The error y is then multiplied by a gain ρ , called partitioning gain, which is defined based on the secondary regulation bandwidth of the k -th generator:

$$\rho_k = \frac{B_{srk} \cdot P_{nk}}{R_S} \quad (36)$$

With equal bandwidths, the error is proportional to the nominal power of the generator.

3.3.4 Power Distribution Among Generators

The aggregated model for a multi-generators system can be rewritten, under the hypothesis of isofrequency, as:

$$\begin{aligned}\Delta P_m &= \sum_k^{N_g} P_{m,k} \\ \Delta P_e &= \sum_k^{N_g} P_{e,k} \\ M \frac{df}{dt} &= \sum_k^{N_g} M_k \frac{df_{COI}}{dt}\end{aligned}$$

The frequency of the center of inertia f_{COI} is the weighted average of the frequency of the generators:

$$f_{COI} = \frac{\sum_k^{N_g} M_k \cdot f_k}{\sum_k^{N_g} M_k} \quad (37)$$

During load changes and the consequent phases of regulation the power is shared among the generators according to their parameters:

Inertial response - at the beginning of the fault only the inertia plays a role in contributing to the power demand change. Under the hypothesis of $E_c \approx 0$, $\Delta f \approx 0$, $\Delta P_m \approx 0$ we can conclude:

$$M \frac{df}{dt} = -\Delta P_e \quad (38)$$

Thus the partitioning is $\frac{\Delta P_{e,k}}{\Delta P_e} = \frac{M_k}{M}$, i.e., the share of inertial power is split among generators according to their inertia. Referring to the definition of $M = T_a \cdot S_n / f_n$ we can conclude that with equal time constants T_a the distribution of power is according to the nominal power of the generators.

Primary regulation response - at steady state the power is shared proportionally to the gain E_p (29).

$$\frac{\Delta P_k}{\Delta P} = \frac{E_{pk}}{E_p} = \frac{1}{E_p} \cdot \frac{P_{nk}}{f_n \cdot b_p} \quad (39)$$

If the statism of generators are equal the power share of primary regulation is again proportional to the nominal power of the generator.

Secondary regulation response - at steady state is, thanks to the centralized regulation, proportional to the bandwidth of each generator participating to secondary regulation. With equal proportion bandwidths the power is shared proportionally to the size of the generators.

3.4 Static Voltage Regulation

As we have shown in chapter 3.2.1, the voltage magnitude depends strongly on reactive power in prevalent inductive system like the DG. The two main ways to regulate voltage through

the control of reactive power are generator excitation control and capacitive/inductive compensators. The other voltage regulation method is through transformer ratio regulation either statically or through the use of on-load tap-changers.

Due to the scope of this thesis we will focus on generator reactive power control.

SGs are equipped with Automatic Voltage Regulator (AVR) which operate on the excitation of the rotor to track the voltage reference at the connection with the grid. There exists a primary level control which focuses on voltage drops of the interconnection transformer and other factors, while a secondary level – which is a centralized voltage regulation – controls the voltage of the HV nodes and shares the reactive power needed among generating units according to negotiated gains.

Grid interfaced static converters have a mandatory capability curve – shown in Fig. 21 – that they need to fulfill according to the annexes A.17 and A.68 of the Italian grid code [10, 15].

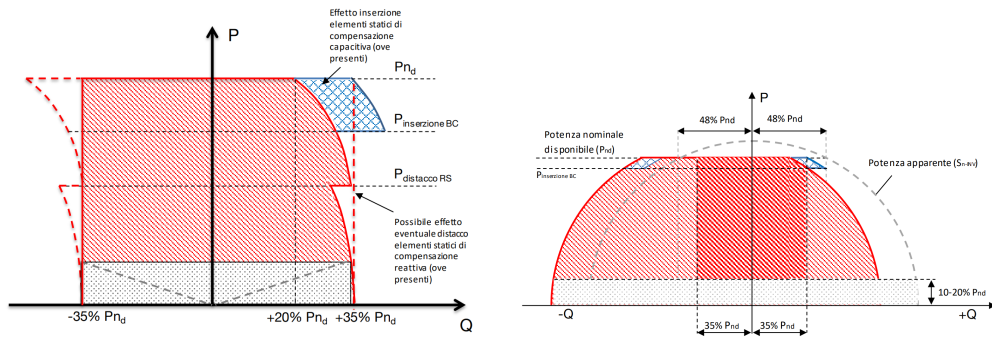


Figure 21: Capability curves of grid interfaced inverters (left) Wind power plants (right) PV powerplants[10, 15].

The grid code allows for a derating of reactive power according to the voltage of the interconnection, Fig. 22 shows the V/Q curve for PV plants.

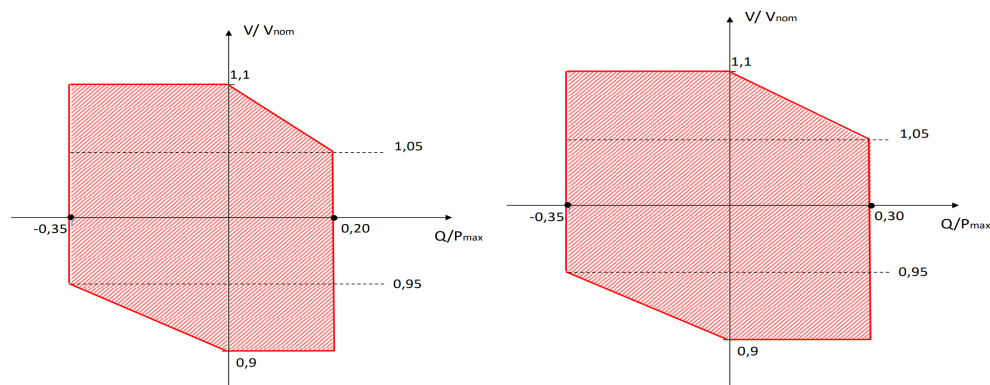


Figure 22: V/Q curve (left) Photovoltaic plants (right) Wind farms [10, 15].

3.5 Dynamic Voltage Regulation

The distribution system must be able to withstand faults in any of its component and continue to function normally. This is why the DS is equipped with breakers who in case of overcurrents – i.e., the fault of system at impressed voltage – open the faulted branch and isolate the fault. Synchronous generators have so far been the main source of fault current in the DS. A short circuited SG at steady state injects a current which is roughly in the order of magnitude of its nominal current, due to the high inductance of the machine. On the opposite, dynamically, due to the tendency of the linked flux to not change, the transient inductance is much smaller (around 0.1 p.u.) and can thus inject high short circuit currents – depending on the location of the fault and thus the fault inductance, even above 5 p.u. – and thus the breakers are able to detect fault currents and trip. Thanks to their high thermal capacity, the overload caused by the fault and the time taken by the breaker to open it, the fault doesn't constitute a problem for the SG.

On the other hand, grid tied inverters have to detect the fault, the control – through its dynamic – has to determine a reactive power based on the droop curves implemented and inject the consequent current. Such procedures take time, but the main issue of grid-tied inverters is the limited overload capability. Overloads on static converter cannot happen for such long times, due to the Si junction of the transistor having such a small thermal capacity that any overload would cause it to reach failure temperatures within tens of milliseconds.

4 Real and Virtual Synchronous Machines

Synchronous generators are electrical machines used to convert mechanical energy into electrical energy. They interface externally through the mechanical shaft, the rotor exciter and the three phases of the stator. The stator phases are usually then connected to a transformer to step up the voltage and inject power in the distribution system as shown in Fig. 23. They have so far been the backbone of the grid and have provided the greater share of grid services like frequency and voltage control.

Stator It's made up of three phase distributed winding, the star center is external to allow grounding

Rotor It contains the exciter winding as well as the damper windings

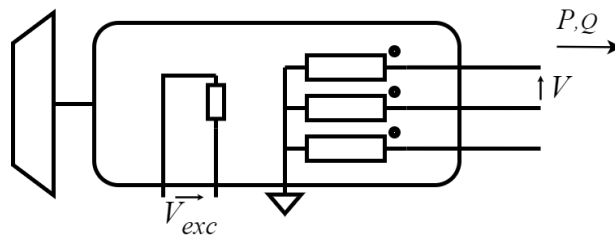


Figure 23: Synchronous generator schematic.

The three phase system can be transformed into a fixed and rotating two phase system thanks to the homopolar component being null; the homopolar component is defined as $x_a + x_b + x_c$. In a star system the current homopolar component is zero thanks to Kirchhoff Current Law (KCL), in a delta system the voltage homopolar component is zero thanks to Kirchhoff Voltage Law (KVL). The axes are represented in Fig. 24.

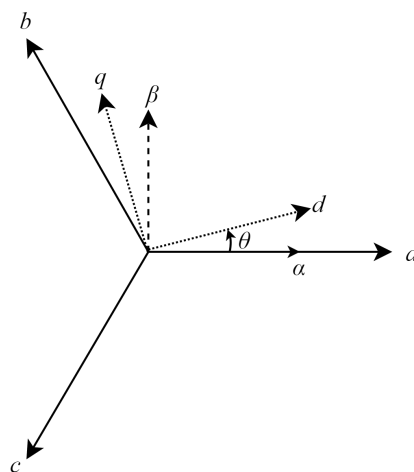


Figure 24: Three and two phase systems.

To project a vector X_{abc} onto the $\alpha\beta$ axes the matrix (40) must be applied:

$$\begin{bmatrix} X_\alpha \\ X_\beta \end{bmatrix} = T_0 \cdot X_{abc} = \begin{bmatrix} 1 & -1/2 & -1/2 \\ 0 & \sqrt{3}/2 & -\sqrt{3}/2 \end{bmatrix} \begin{bmatrix} X_a \\ X_b \\ X_c \end{bmatrix} \quad (40)$$

The vector $X_{\alpha\beta}$ is though scaled by $3/2$, to account for this the matrix (40) can be scaled by $2/3$; the consequent power in the $\alpha\beta$ axes will then have to be scaled by $3/2$ to account for the different number of phases and the re-scaling:

$$\begin{bmatrix} X_\alpha \\ X_\beta \end{bmatrix} = T \cdot X_{abc} = \begin{bmatrix} 2/3 & -1/3 & -1/3 \\ 0 & 1/\sqrt{3} & -1/\sqrt{3} \end{bmatrix} \begin{bmatrix} X_a \\ X_b \\ X_c \end{bmatrix} \quad (41)$$

The inverse transformation is instead obtained through matrix (42):

$$\begin{bmatrix} X_a \\ X_b \\ X_c \end{bmatrix} = T^{-1} \cdot X_{\alpha\beta} = \begin{bmatrix} 1 & 0 \\ -1/2 & \sqrt{3}/2 \\ -1/2 & -\sqrt{3}/2 \end{bmatrix} \begin{bmatrix} X_\alpha \\ X_\beta \end{bmatrix} \quad (42)$$

To rotate the $\alpha\beta$ axes onto the dq axes instead it's necessary to apply the rotation transformation shown in (43):

$$\begin{bmatrix} X_d \\ X_q \end{bmatrix} = R \cdot X_{\alpha\beta} = \begin{bmatrix} \cos(\theta) & \sin(\theta) \\ -\sin(\theta) & \cos(\theta) \end{bmatrix} \begin{bmatrix} X_\alpha \\ X_\beta \end{bmatrix} \quad (43)$$

By re-writing the equations of the $\alpha\beta$ and dq axes in the complex form: $x_\alpha + jx_\beta$, $x_d + jx_q$ we can write (43) as:

$$X_{dq} = e^{-j\theta} X_{\alpha\beta} \quad (44)$$

Given the orthonormal propriety of the R matrix, its inverse corresponds to the transpose $R^{-1} = R'$; the inverse transformation in complex form is $e^{j\theta}$.

By approximating the linked flux to the fundamental harmonic it is possible to define two inductances in the dq reference frame, as shown in Fig. 25. Given that the phase shift between the axes is 90° we can conclude the absence of mutual interaction between the two, there exists though a mutual Electromotive Force (EMF) due to the axes transformation. The inductances L_d and L_q are equal in the case of isotropic rotors.

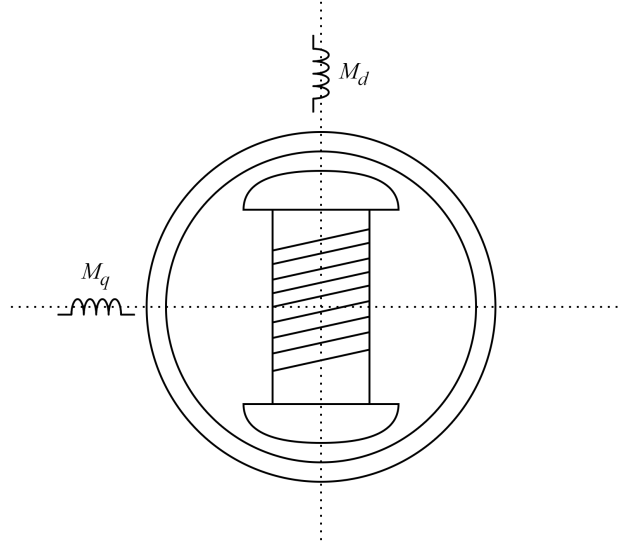


Figure 25: Electrical schematic of the generator's dq axes.

The equations yielded by the process already defined – whose demonstration is beyond the scope of this thesis – can be recollected as:

$$v_d = -R_s i_d + \frac{d\lambda_d}{dt} - w_e \lambda_q \quad (45)$$

$$v_q = -R_s i_q + \frac{d\lambda_q}{dt} + w_e \lambda_d \quad (46)$$

$$v_e = R_e i_e + \frac{d\lambda_e}{dt} \quad (47)$$

$$R_{rd} i_{rd} + \frac{d\lambda_{rd}}{dt} = 0 \quad (48)$$

$$R_{rq} i_{rq} + \frac{d\lambda_{rq}}{dt} = 0; \quad (49)$$

The electrical representation is depicted in Fig. 26:

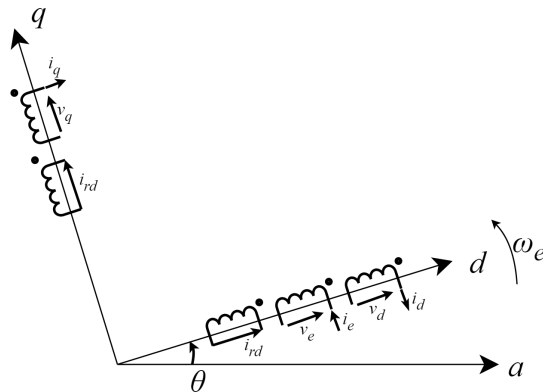


Figure 26: Electrical schematic of the dq axes.

The stator equations can be re-written in complex form ($\bar{v} = v d + j v q$), the result is:

$$\bar{v} = -R_s \bar{i} + \frac{d\bar{\lambda}}{dt} + j w_e \bar{\lambda} \quad (50)$$

The flux equations under no damping conditions can be analytically reduced to:

$$\begin{aligned}\lambda_d &= -L_d i_d + M i_e \\ \lambda_q &= -L_q i_q \\ \lambda_e &= L_e i_e - M i_d\end{aligned}\tag{51}$$

$$\begin{cases} L_d = \frac{3}{2}M_d + L_{\sigma_s} \\ L_q = \frac{3}{2}M_q + L_{\sigma_s} \\ M = \sqrt{\frac{3}{2}}M_d \\ L_e = M_d + L_{\sigma_r} \end{cases}\tag{52}$$

M_d and M_q are the inductances of the dq axes as represented in Fig. 26 while L_{σ} is the stray inductance of the stator and rotor windings.

The damper windings are instead based on the method used to damp the generator, and are thus not represented in this formulation.

The steady state equation derived from (50), and obtained by neglecting the resistance – as is proper in power plant SGs – can be written as (53), and its circuitual representation is in Fig. 27:

$$\bar{E} = jX\bar{I} + \bar{V}\tag{53}$$

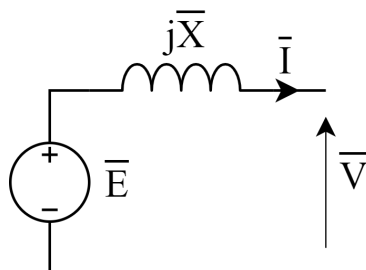


Figure 27: Circuitual representation of a steady state synchronous generator.

4.1 Virtual Synchronous Machine

The Virtual Synchronous Machine (VSM) is an algorithm that, through the equations of Synchronous Generators, make grid-tied inverters behave as or even better than a conventional synchronous machine. A scheme of a inverter interfaced to the grid through an LCL filter is shown in Fig. 28. The dc voltage can be sourced from renewable sources, storage or car batteries in the case of V2G technology.

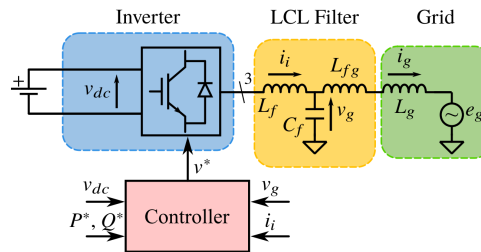


Figure 28: Grid interfaced inverter schematic [16].

The inverter control system measures the current output i_i , the line-line (or line-neutral) voltage across the capacitors v_g and the dc-link v_{dc} .

The dynamic of a Virtual Machine is related to the phenomena at the fundamental frequency (i.e., 50 Hz). Consequently, the dynamic of a VSM does not interfere with the phenomena related to the switching frequency (order of kHz). Therefore, the modulation strategies are all equivalent to each other as far as the mean values are concerned. Moreover, such independence allows to perform simulations as mean values instead of instantaneous ones.

Starting from 2007 several VSM solutions have been proposed in literature and they are divided into two main categories, voltage and current controlled:

- **Voltage Source**

- VISMA II [17]
- Synchroverter Base [18]
- Synchroverter Self-sync [19]
- Osaka [20]

- **Current Source**

- VISMA [21]
- VISMA I [22]
- Further Synchroverter [23]
- SPC [24]
- KHI [25]
- VSYNC [26]
- CVSM [27]
- S-VSC [28]

4.2 S-VSC

Fig. 29 represents the possible options to the control of the S-VSC analyzed in this thesis. As it can be observed, the inputs are an active and reactive power set-point and the option

to add a droop control for frequency and voltage control; these are then fed either to the Inverter or the S-VSC depending on the control (Table 3).

The S-VSC is the source of grid synchronization for the current control (with the virtual rotor angle θ_r). In fact, thanks to the inertia of the virtual rotor, the S-VSC provides a stable and filtered grid angle measurement. Therefore, a PLL is not needed for the operation. [16]

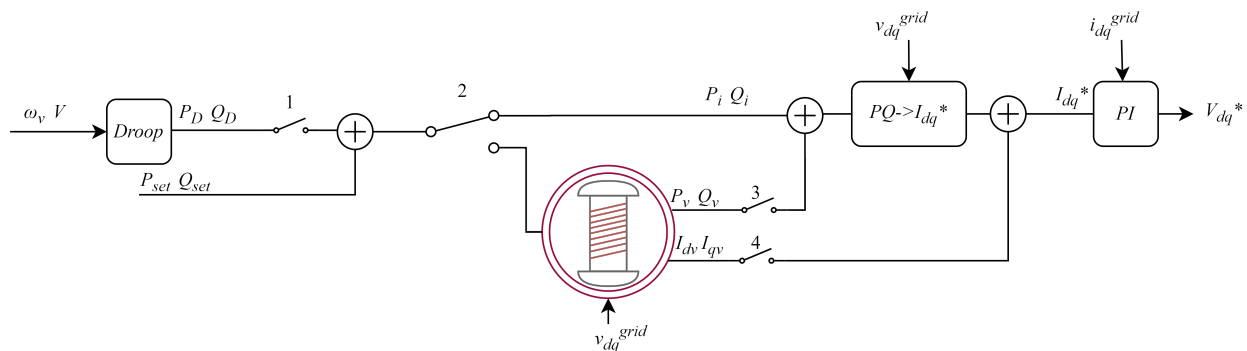


Figure 29: S-VSC control schematic.

The control can be divided into Simplified - Virtual Synchronous Compensator (S-VSC) or Simplified - Virtual Synchronous Generator (S-VSG). Moreover the setup designed can also work as a traditional Voltage Source Inverter (VSI) which instead of a Phase Locked Loop (PLL) uses the virtual speed of the generator as reference.

The references from the S-VSM can be passed onto the inverter as powers (P_v, Q_v) or currents (I_{dv}, I_{qv}). The effects of either will be detailed in the experimental results.

Operating mode	Switch 2	Switch 3	Switch 4
VSI	up	off	off
S-VSG PQ	down	on	off
S-VSG I_{dq}	down	off	on
S-VSC PQ	up	on	off
S-VSC I_{dq}	up	off	on

Table 3: CONTROL SCHEME OF THE S-VSM.

VSI The VSI is a representation of the most common control of grid tied inverters. It can perform droop control both on active and reactive power and/or injecting constant powers into the grid. It is analyzed to carry out a comparison with the VSM behavior;

VSG The VSG is the simplest implementation of the VSM, all the power demands are fed into a virtual model of the machine and the power output are fed into the inverter. The drawbacks are a weaker dynamic behavior compared to the VSC proposed in [16];

VSC The VSC is a control in which the set-point powers of the virtual machine are always zero. This means that both droop control and set-point power are directly fed to the inverter through the transformation in equation (58). This control implies that the VSM operates, at steady state, at no load. This has positive effects on its

synchronizing power and dynamics, seen that the behavior of the machine is different depending on the working point.

The S-VSC is therefore a voltage-input, power-output model. The input voltage v_g is measured across the LCL filter capacitor C_f . The S-VSM is organized in several blocks, each in charge of a specific aspect of the VSM:

Power conversion This block calculates the virtual power of the machine;

Mechanical emulation This blocks simulates the inertia of the machine and outputs the virtual speed and angle of its rotor;

Machine equations This block implements the equations of the stator; from these virtual powers and currents are calculated;

Excitation equations The virtual excitation flux control for reactive support during faults and short circuit current injection.

4.2.1 Power Conversion

The active and reactive virtual power are obtained by the measured grid voltage v_g and the virtual currents $i_{v,dq}$ (54).

The reference dq currents for the control loop are then calculated using (55)

$$P_v + jQ_v = \frac{3}{2} \cdot \bar{v}_{g,dq} \cdot \bar{i}_{v,dq}^* \quad (54)$$

$$i_{dq}^{ref} = \frac{2}{3} \frac{P_i + P_v - j(Q_i + Q_v)}{v_d - jv_q} \quad (55)$$

By adopting the per unit values: S_b for base power, V_n for peak phase voltage (phase-neutral) and f_b for 50 Hz, we can derive the remaining values as follows

$$I_b = \frac{2S_b}{3V_b} \quad Z_b = \frac{V_b}{I_b} \quad L_b = \frac{Z_b}{\omega_b} \quad C_b = \frac{1}{\omega Z_b} \quad (56)$$

This allows us to simplify the power equation to $P + jQ = VI^*$ and remove the scaling factor of 3/2; this will be the convention adopted from now on.

The current reference in p.u. is then:

$$i_{dq}^{ref} = \frac{P_i + P_v - j(Q_i + Q_v)}{v_d - jv_q} \quad (57)$$

The VSM references can also be used directly in the form of currents in the dq axes as shown in Table 3. In this case the reference currents are calculated as shown in (58). The major difference in the approaches is that P_v and Q_v are influenced by the dynamics of the Point of Common Coupling (PCC) voltage, meanwhile virtual currents $I_{v,dq}$ are slowed down to the inductance of the generator, thus yielding a different dynamic behavior.

$$i_{dq}^{ref} = \frac{P_i - jQ_i}{v_d - jv_q} + i_{v,d} + ji_{v,q} \quad (58)$$

4.2.2 Mechanical Emulation

The mechanical emulation is the key component of the VSM, as it provides the synchronization with the grid and both the frequency – interpreted also as an angular velocity ω_r – and the rotor angle θ_r .

The starting formula for the rotor equation is the swing equation (59):

$$P_m - P_e = 2H \frac{d(\omega_r - \omega_g)}{dt} + D_p(\omega_r - \omega_g) \quad (59)$$

The mechanical power P_m becomes the reference virtual power P_v^* while the electrical power is the P_v calculated according to equation (54). The result is shown in Fig. 30.

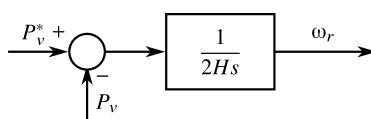


Figure 30: Simplified swing equation of the VSM [16].

4.2.3 Machine Equations

The electrical equations of the S-VSM simulate a virtual stator in the dq rotating frame, they also include the possibility of a simplified damper in the q axis, as it will be described in chapter 4.3.

Like in real machines, the excitation flux acts on the d axis, while the q axis is responsible for active power (Torque). If the d axis were alligned to the voltage vector the convention of active and reactive power would be reversed.

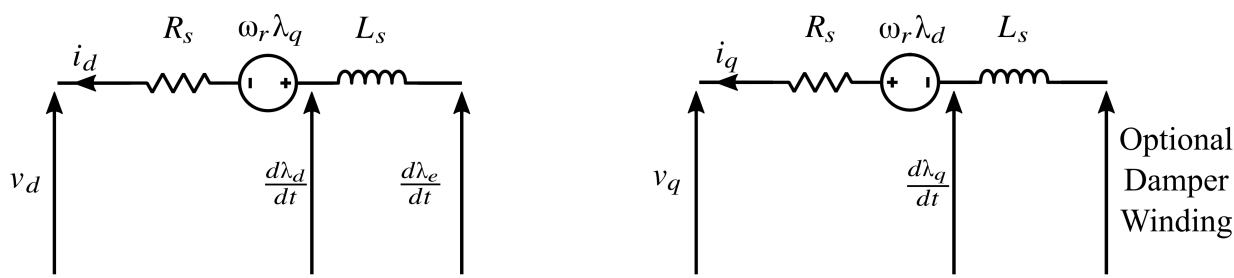


Figure 31: Equivalent circuits in the dq axes. (left) d -axis (right) q -axis [16].

The non-linearities of real SGs are ignored. This allows us to directly relate linked flux to inductance and current. All the inherent dampings of the SGs – except the optional damper winding – have been neglected too.

The resulting equations (60) and (61) are in p.u. value, R_s is the stator resistance, λ_d and λ_q are the stator linked flux, ω_b is the base speed.

$$v_d = -R_s i_d - \omega_b \lambda_q + \frac{1}{\omega_b} \frac{d\lambda_d}{dt} \quad (60)$$

$$v_q = -R_s i_q + w \lambda_d + \frac{1}{w} \frac{d\lambda_q}{dt} \quad (61)$$

Thanks to the linearities, the current can be derived as shown in (62),(63). Equation (63) does not include the damping winding linked flux, the corrected term will be introduced in chapter 4.3.

$$i_d = \frac{\lambda_e - \lambda_d}{L_s} \quad (62)$$

$$i_q = -\frac{\lambda_q}{L_s} \quad (63)$$

4.2.4 Excitation Control

The S-VSC control uses an integral control for the excitation, where Q_v^* is the reference reactive power for the machine. In the VSC control the reference reactive power is always zero $Q_v^* = 0$; while in the VSG mode it is set by the voltage control and set-point. The control scheme proposed in [16] is represented in Fig. 32. The control implements a feed-forward control λ_{ff} . This term depends on the external reactive power set-point of the converter and the grid inductance L_g , which is estimated by the control \tilde{L}_g .

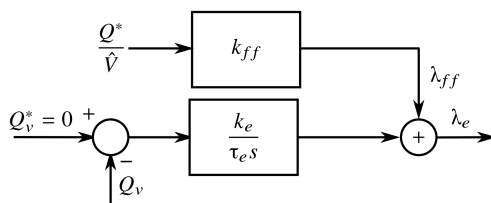


Figure 32: Excitation control block [16].

To carry out the study of the excitation control, a linearized problem is devised under the following hypotheses:

- The system is supposed to be connected to the MV or HV grid, thus the connection is mainly reactive; the grid resistance R_g is therefore neglected;
- The stator resistance is neglected $R_s \simeq 0$;
- The virtual rotor speed is assumed constant for the small signal analysis $\omega_r \simeq \omega_0$ with $\omega_0 = 1$;
- The derivatives of the flux linkages of the virtual machine are negligible $\frac{d\lambda}{dt} \simeq 0$;
- The inner current controller is considered ideal, and therefore the actual inverter current is always equal to its reference.

The equation for the stator, under the aforementioned hypotheses, are as follows:

$$j\omega_r \lambda_{dq} = e_g^{dq} + \omega_0 L_g i_v^{dq} \quad (64)$$

Thanks to the non-interaction between the flux linkages of the dq axes and thanks to the fact that the excitation insists only in the d axis, the q axis equations of (64) are neglected, leading to equation (65).

$$\omega_0 \lambda_d = e_g^q + L_g i_v^d \quad (65)$$

4.3 Electromechanical Damping

As it is shown in this chapter, due to the power being proportional to the phase shift, non damped generators will oscillate around the equilibrium point. These oscillations can lead to a step loss, this is a phenomenon where the generator shifts of 180° , the transient currents deriving from the phenomenon can lead to the trip of protections and the generator disconnection.

Under the linearized hypotheses of chapter 3.2.1 and 3.3, we can write the linearized swing equation of the generator as

$$2H \frac{d\Delta\omega}{dt} = \Delta P_m - \Delta P_e \quad (66)$$

$$\frac{d\delta}{dt} = \omega_n (\omega_v - \omega_0) \quad (67)$$

$$\Delta P_e = \frac{E' E_g}{X' + X_g} \sin(\Delta\delta) = P'_{max} \sin(\Delta\delta) \quad (68)$$

Under the small angle approximation we can linearise the electrical power as a function of the synchronizing power defined in (69)

$$\Delta P_e = P'_{s0} \Delta\delta \quad \rightarrow \quad P'_{s0} \equiv \frac{\Delta P_e}{\Delta\delta} = P'_{max} \cos(\delta_0) \quad (69)$$

The final dynamical system is therefore

$$2H \frac{d\Delta\omega}{dt} = \Delta P_m - P'_{s0} \Delta\delta \quad (70)$$

$$\frac{d\Delta\delta}{dt} = \omega_n \Delta\omega \quad (71)$$

We can now proceed to write the matrix representation of the linear system, through the calculation of the eigenvalues we can derive the oscillation period of the generators.

$$\begin{bmatrix} \Delta\dot{\omega} \\ \Delta\dot{\delta} \end{bmatrix} = \begin{bmatrix} 0 & -\frac{P'_{s0}}{2H} \\ \omega_n & 0 \end{bmatrix} + \begin{bmatrix} \Delta P_m \\ 0 \end{bmatrix} \quad (72)$$

By evaluating the eigenvalues, $\det(A - \lambda I) = 0$, we obtain the period of oscillation in (74):

$$\det \left(\begin{bmatrix} -\lambda & -\frac{P'_{s0}}{2H} \\ \omega_n & -\lambda \end{bmatrix} \right) = 0 \quad \rightarrow \quad \lambda^2 + \frac{P'_{s0} \omega_n}{2H} = 0 \quad (73)$$

$$\lambda_{1,2} = \pm j \sqrt{\frac{P'_{s0} \omega_n}{2H}} \quad (74)$$

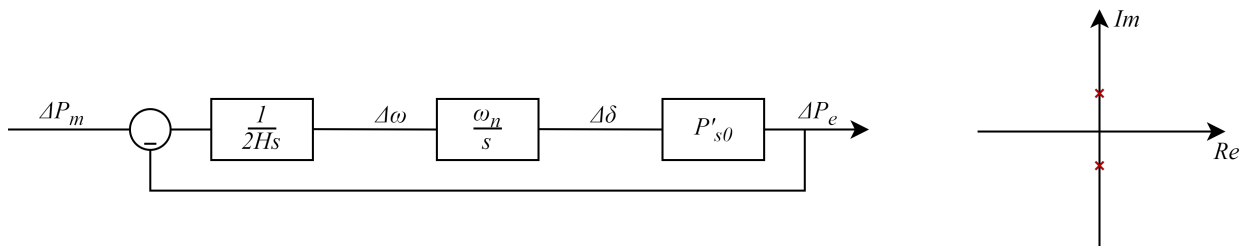


Figure 33: Transfer function block and pole representation of the undamped system.

These oscillations then require a damping method both in real generators and virtual ones. Real SGs are equipped with dampening winding that act as a squirrel cage in the induction motor, creating a torque proportional to the slip speed.

The methods proposed in literature for the VSM are:

Droop-based damping: it emulates traditional SG damper winding, the damping is proportional to the virtual slip speed [29].

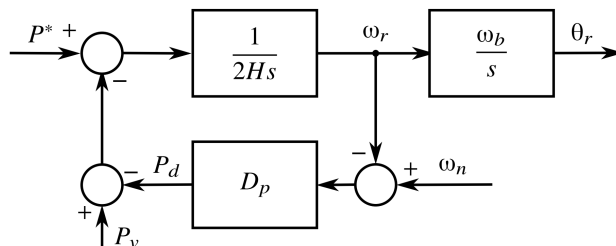


Figure 34: Droop control block diagram [16].

PLL-based damping: a proportional damper referenced to the measured grid frequency [30].

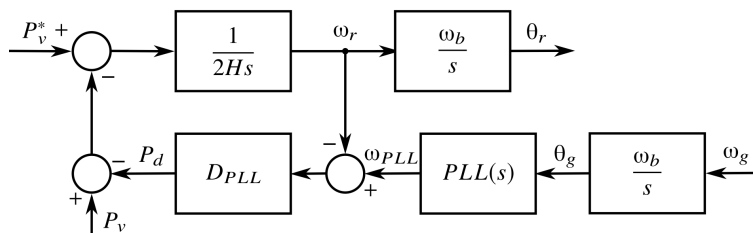


Figure 35: PLL control block diagram [16].

PI-based damping: a PI regulator is used in place of the machine virtual speed regulator.

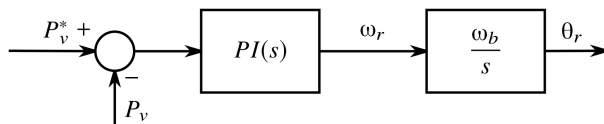
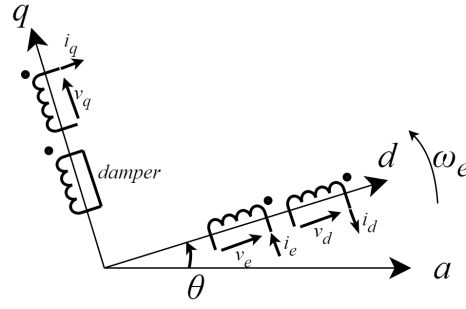


Figure 36: PI control block diagram [16].

RQ-based damping: emulates a damper winding on the q -axis [31]. The mechanical control block in Fig. 38 is unchanged.

Figure 37: dq axes winding schematic.

The equations of the machine have an added term in the q axis due to the additional winding added, they can be rewritten as:

$$v_d = -R_s i_d - w_r \lambda_q + \frac{1}{w} \frac{d\lambda_d}{dt} \quad (75)$$

$$v_q = -R_s i_q + w_r \lambda_d + \frac{1}{w} \frac{d\lambda_q}{dt} \quad (76)$$

$$\frac{L_{rq}}{\omega_b R_{rq}} \frac{d\lambda_{rq}}{dt} = -\lambda_{rq} - L_{rq} i_{rq} \quad (77)$$

$$i_d = \frac{\lambda_e - \lambda_d}{L_s} \quad (78)$$

$$i_q = \frac{\lambda_{rq} - \lambda_q}{L_s} \quad (79)$$

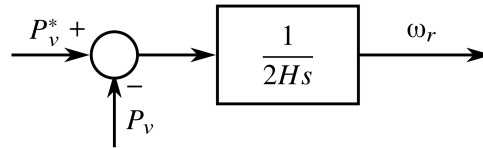


Figure 38: RQ control block diagram [16].

Lead Lag-based damping: a lead lag filter on the virtual active power of the machine [32].

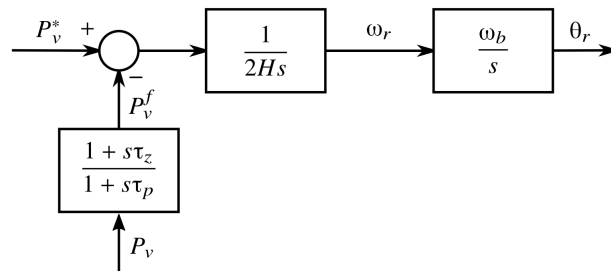


Figure 39: LL control block diagram [16].

5 Laboratory Setup

To validate the control described so far, the laboratory test setup in Fig. 40 has been used. This is both to evaluate the correctness of the theoretical results and to verify the hypotheses and simplification done during the analytical study.

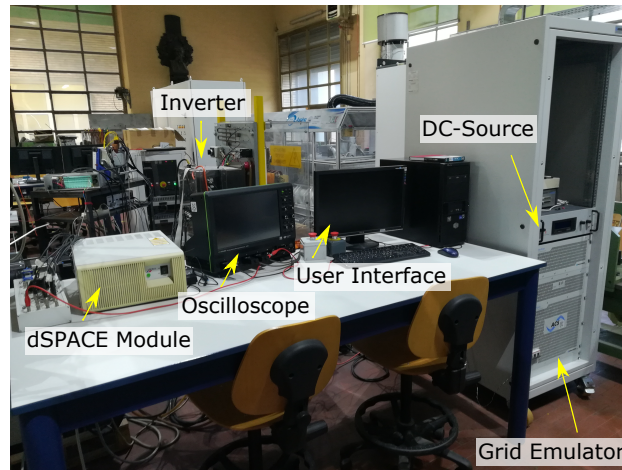


Figure 40: Laboratory control desk.

The laboratory tests were preceded by extensive simulations using PLECS, the first simulation were conducted using a static grid. This is the simplest setup devised, it allows us to evaluate the grid synchronization, the behavior of the control and on top of this the setup allows us to see how the inverter reacts to a stiff grid, i.e., a grid whose behavior is unchanged by the actions of the inverter. This is the case of small power grid interfaced inverters or medium sized converters interfaced to the HV distribution grid.

The laboratory tests are divided into these main categories:

Single inverter with variable grid: This setup emulates a grid with a high share of renewable energy sources simulated within a two bus systems. In this test the grid is perceptible to the effects of the converters connected to it. Therefore, this setup allows to evaluate the impact of the system inertia on the grid's frequency and the response to perturbations and faults.

Two inverters with variable grid: The tests, similar to the one conducted with a single inverter, allows to see the behavior of two systems operating in parallel within the same setup. Problems could ensue from the interaction between the two controls, this is why it is necessary to evaluate the results.

Microgrid with variable grid: The system is made up of three inverters interconnected and interfaced with the grid. The system can let us see the behavior of the three separate sources to faults and contingencies; moreover, it can show the behavior of different control strategies and different parameters on the virtual machines.

Islanding: The test focuses on the ability of the microgrid to remain stable on its own after an hypothetical fault of the main DN, this ability represents one of the most

important and appreciate feature of microgrids. The tests verify the stability of the system during the disconnection and the steady state conditions.

5.1 Grid interfaced Three phase Inverter

The control loop described so far is implemented into a laboratory setup consisting of three inverters called R1, G1 and G2.

5.1.1 R1 Inverter

The R1 is a system consisting of a dc-dc converter and a dc-ac converter, as shown in Fig. 41. The dc-dc stage is supplied by a 15 kW dc source at 300 V and operates as a boost converter stepping up the voltage to the desired dc-link voltage of 400 V. Next, the bidirectional three phase inverter uses IGBT switches modulating at 10 kHz, shown in Fig. 41. The dc-ac converter is interfaced to the grid through an LCL filter shown in Fig. 42, this is to provide the converter the necessary output inductance and to further dampen the output voltage and current ripple. The inverter is programmed and interfaced with the dSPACE control platform, which allows data acquisition and virtual scopes to monitor the signals sent and received from the inverter i.e., phase currents, voltages, duty cycles, VSM frequency etc.

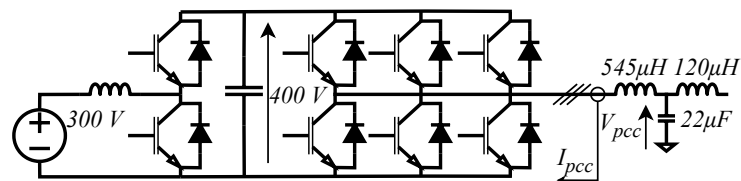


Figure 41: Electrical schematic of the grid interfaced R1 inverter.

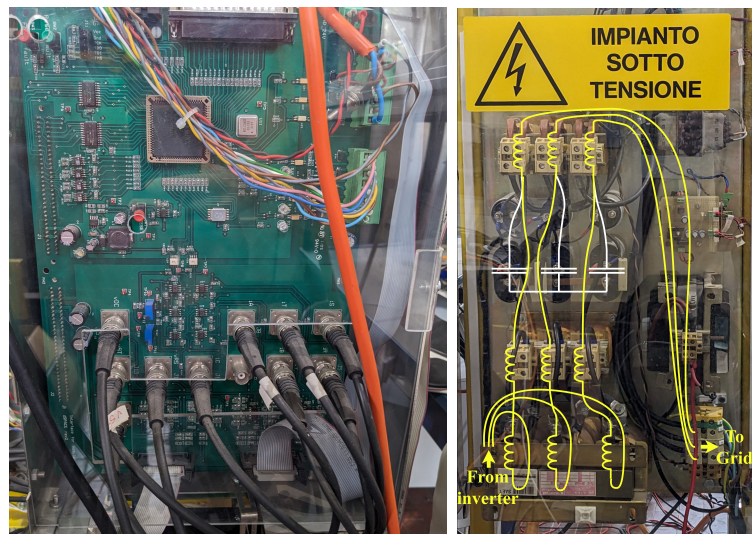


Figure 42: (left) R1 Inverter interface to dSPACE control unit (right) inverter LCL filter.

5.1.2 G1 & G2 Inverters

The two inverters G1 and G2 are identical, they are supplied by a 650 V DC source and can thus work at higher grid V_{RMS} , in our case 208 V_{RMS} ; the switching frequency is set at 10 kHz like the R1 converter.

The grid LCL filter, given the higher voltages, has different values of inductances and capacitance, shown in Fig. 43.

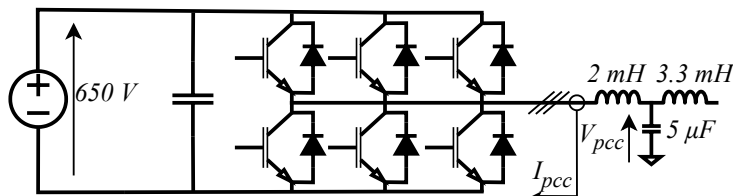


Figure 43: Electrical schematic of the grid interfaced G1 and G2 inverters.

Fig. 44 shows the physical inverter interface and filtering stage.

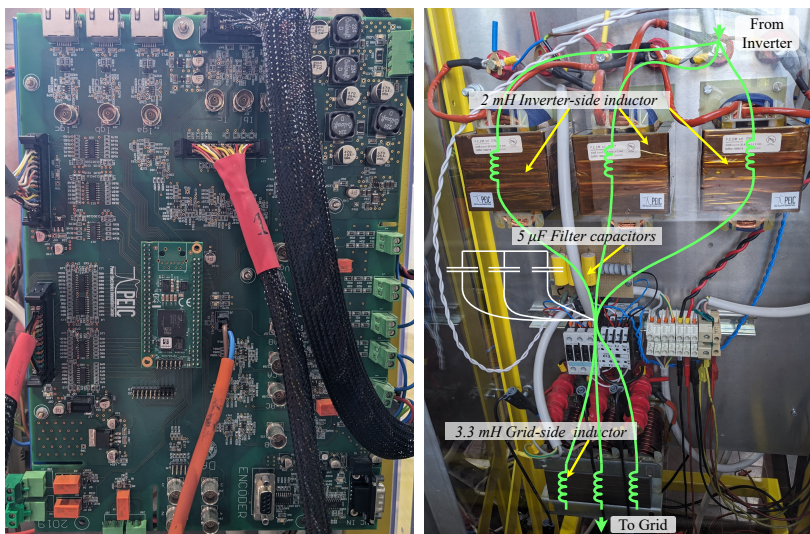


Figure 44: (left) G1 and G2 Inverter interface to dSPACE control unit (right) inverter LCL filter.

5.2 Grid Emulator and Microgrid Transformer

This section describes the power apparatus used to closely emulate the real DG, it consist of a 50kVA transformer and grid emulator of Fig. 45 wired as shown in Fig. 53.

The grid emulator is a four quadrant three phase inverter, the converter works in amplification mode, i.e., it receives three analog signals and amplifies them to the desired voltage and absorbs the consequent current.

The transformer is wired in a star delta configuration (\star/Δ), with a turn ratio of 3:1, this results in a primary star voltage of $120 V_{RMS}^{\star}$ and a secondary delta voltage of $360 V_{RMS}^{\Delta}$,

which is equal to the star voltage of $208 V_{RMS}^{\wedge}$

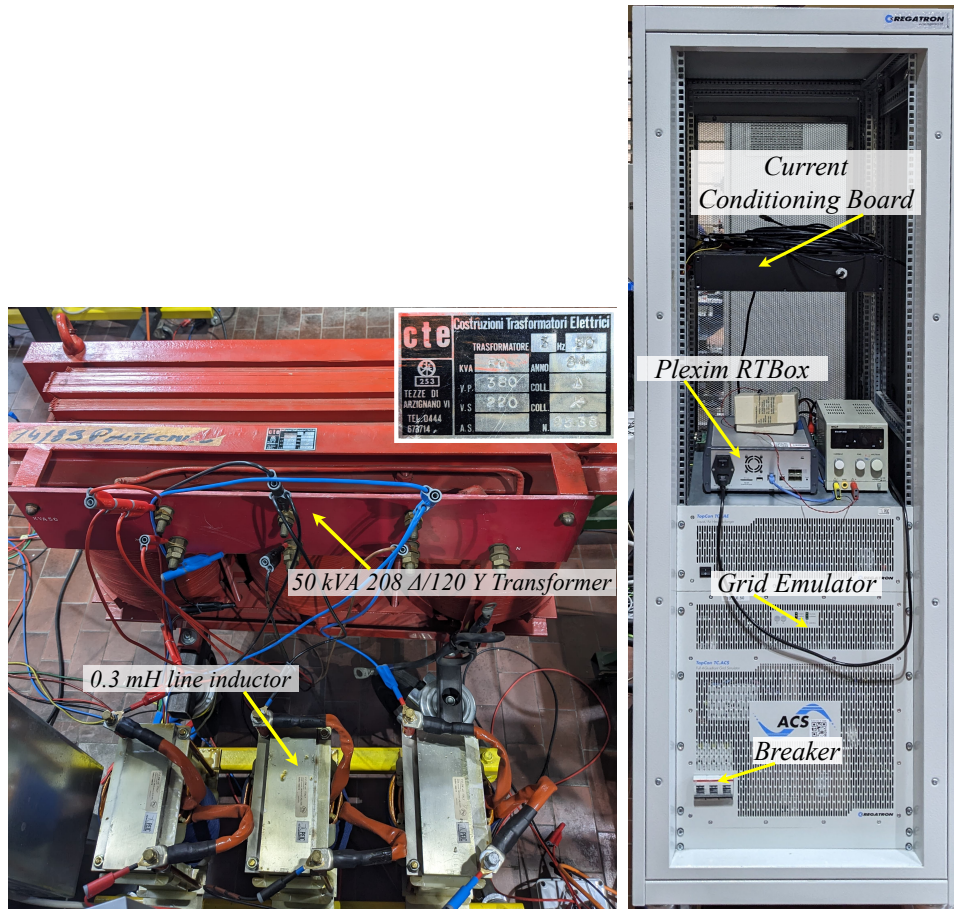


Figure 45: (left) Transformer (right) grid emulator.

6 Personal Contributions to the Laboratory Setup

The setup used to carry out the experiments in this thesis had the necessity to be modified and updated to function; and the microgrid needed to be assembled in its entirety.

6.1 G1 & G2 Inverter Refurbishment

The G1 and G2 inverters have undergone a period of refurbishment in which the analogue and digital connectors were rewired, and the code was updated to handle two simultaneous VSMs running.

The Pinout of the dSPACE connectors is the following:






















































dSpace Port	dSpace Pin #	Pin Name	Unit	Signal	Peripheral	Guasch Name	Pin J26	Color
Digital A	17	DIO1 ch1	1	T1	PWM Unit	BIT_OUT_DSPACE.0	18	
	16	DIO1 ch2		T2		BIT_OUT_DSPACE.1	20	
	15	DIO1 ch3		T3		BIT_OUT_DSPACE.2	22	
	14	DIO1 ch4		T4		BIT_OUT_DSPACE.3	24	
	13	DIO1 ch5		T5		BIT_OUT_DSPACE.4	26	
	12	DIO1 ch6		T6		BIT_OUT_DSPACE.5	28	
	11	DIO1 ch7		Awake	DIO	BIT_OUT_DSPACE.6	15	
	10	DIO1 ch8		PWMLEN	DIO	BIT_OUT_DSPACE.7	13	
	5	DIO1 ch13		EMPTY	-	BIT_OUT_DSPACE.8	11	
	9	DIO1 ch9		MISO	SPI	BIT_OUT_DSPACE.5	6	
	8	DIO1 ch10		CLK		BIT_OUT_DSPACE.9	9	
	7	DIO1 ch11		MOSI		BIT_OUT_DSPACE.10	7	
	6	DIO1 ch12		CS	GND	BIT_OUT_DSPACE.11	5	
	18	GND		GND		GND	3	
	19	GND		GND		GND	4	
	1	GND		GND	GND	30		
	4	DIO1 ch14		Fault T1	DIO	BIT_IN_DSPACE.0	16	
	3	DIO1 ch15		Fault T2		BIT_IN_DSPACE.1	14	
	2	DIO1 ch16		Fault T3		BIT_IN_DSPACE.2	12	
	49	DIO1 ch17		Fault T4		BIT_IN_DSPACE.3	10	
	48	DIO1 ch18		Fault T5		BIT_IN_DSPACE.4	8	
	47	DIO1 ch19		Fault T6		BIT_IN_DSPACE.6	17	
	46	DIO1 ch20		Fault T7		BIT_IN_DSPACE.7	19	
	45	DIO1 ch21		An Fault		BIT_IN_DSPACE.8	21	
44	DIO1 ch22	Gen Fault	BIT_IN_DSPACE.9	23				
43	DIO1 ch23	-	BIT_IN_DSPACE.10	25				
42	DIO1 ch24	dSpace Off	BIT_IN_DSPACE.11	27				
Digital B	14	DIO1 ch36	2	T1	PWM Unit	BIT_OUT_DSPACE.0	18	
	13	DIO1 ch37		T2		BIT_OUT_DSPACE.1	20	
	12	DIO1 ch38		T3		BIT_OUT_DSPACE.2	22	
	11	DIO1 ch39		T4		BIT_OUT_DSPACE.3	24	
	10	DIO1 ch40		T5		BIT_OUT_DSPACE.4	26	
	9	DIO1 ch41		T6		BIT_OUT_DSPACE.5	28	
	8	DIO1 ch42		Awake	DIO	BIT_OUT_DSPACE.6	15	
	7	DIO1 ch43		PWMLEN	DIO	BIT_OUT_DSPACE.7	13	
	6	DIO1 ch44		EMPTY	-	BIT_OUT_DSPACE.8	11	
	5	DIO1 ch45		MISO	SPI	BIT_OUT_DSPACE.5	6	
	4	DIO1 ch46		CLK		BIT_OUT_DSPACE.9	9	
	3	DIO1 ch47		MOSI		BIT_OUT_DSPACE.10	7	
	2	DIO1 ch48		CS	GND	BIT_OUT_DSPACE.11	5	
	1	GND		GND		GND	3	
	33	GND		GND		GND	4	
	50	GND		GND	GND	30		
	Digital A	41		DIO1 ch25	Fault T1	DIO	BIT_IN_DSPACE.0	16
40		DIO1 ch26	Fault T2	BIT_IN_DSPACE.1	14			
39		DIO1 ch27	Fault T3	BIT_IN_DSPACE.2	12			
38		DIO1 ch28	Fault T4	BIT_IN_DSPACE.3	10			
37		DIO1 ch29	Fault T5	BIT_IN_DSPACE.4	8			
36		DIO1 ch30	Fault T6	BIT_IN_DSPACE.6	17			
35		DIO1 ch31	Fault T7	BIT_IN_DSPACE.7	19			
34		DIO1 ch32	An Fault	BIT_IN_DSPACE.8	21			
Digital B	17	DIO1 ch33	Gen Fault	BIT_IN_DSPACE.9	23			
	16	DIO1 ch34	-	BIT_IN_DSPACE.10	25			
	15	DIO1 ch35	dSpace Off	BIT_IN_DSPACE.11	27			

Table 4: DIGITAL PINOUT OF dSPACE.




















































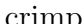
dSpace Port	dSpace Pin #	Pin Name	Unit	Signal	Peripheral	Guasch Name	Pin J26	Color
Analog A	17	AI1 ch1	1	V_{dc}	ADC	VDC	1	
	33	<u>AI1 ch1</u>		V_{dc}		GND_A	2	
	49	AI1 ch2		I_a		Ia	3	
	16	<u>AI1 ch2</u>		I_a		GND_A	4	
	32	AI1 ch3		I_b		Ib	5	
	48	<u>AI1 ch3</u>		I_b		GND_A	6	
	15	AI1 ch4		I_c		Ic	7	
	31	<u>AI1 ch4</u>		I_c		GND_A	8	
	47	AI1 ch5		V_{gca}		Vgca	10	
	14	<u>AI1 ch5</u>		V_{gca}		GND_A	12	
	30	AI1 ch6		V_{gbc}		Vgbc	12	
	46	<u>AI1 ch6</u>		V_{gbc}		GND_A	11	
	13	AI1 ch7		V_{gab}		Vgab	14	
	29	<u>AI1 ch7</u>		V_{gab}		GND_A	13	
	45	AI1 ch8		V_{cca}		Vcca	16	
	12	<u>AI1 ch8</u>		V_{cca}		GND_A	15	
	28	AI1 ch9		V_{cbc}		Vcbc	18	
	44	<u>AI1 ch9</u>		V_{cbc}		GND_A	17	
	11	AI1 ch10		V_{cab}		Vcab	20	
	27	<u>AI1 ch10</u>		V_{cab}		GND_A	19	
	43	AI1 ch11		I_{ga}		Iga	21	
	10	<u>AI1 ch11</u>		I_{ga}		GND_A	22	
	26	AI1 ch12		I_{gb}		Igb	23	
	42	<u>AI1 ch12</u>		I_{gb}		GND_A	24	
	9	AI1 ch13		I_{gc}		Igc	25	
	25	<u>AI1 ch13</u>		I_{gc}		GND_A	26	
Analog A	41	AI1 ch14	2	V_{dc}	ADC	VDC	1	
	8	<u>AI1 ch14</u>		V_{dc}		GND_A	2	
	24	AI1 ch15		I_a		Ia	3	
	40	<u>AI1 ch15</u>		I_a		GND_A	4	
	7	AI1 ch16		I_b		Ib	5	
	23	<u>AI1 ch16</u>		I_b		GND_A	6	
	39	AI1 ch17		I_c		Ic	7	
	6	<u>AI1 ch17</u>		I_c		GND_A	8	
	-	-		V_{gca}		Vgca	10	
	-	-		V_{gca}		GND_A	12	
	22	AI1 ch18		V_{gbc}		Vgbc	12	
	38	<u>AI1 ch18</u>		V_{gbc}		GND_A	11	
	5	AI1 ch19		V_{gab}		Vgab	14	
	21	<u>AI1 ch19</u>		V_{gab}		GND_A	13	
	37	AI1 ch20		V_{cca}		Vcca	16	
	4	<u>AI1 ch20</u>		V_{cca}		GND_A	15	
	20	AI1 ch21		V_{cbc}		Vcbc	18	
	36	<u>AI1 ch21</u>		V_{cbc}		GND_A	17	
	3	AI1 ch22		V_{cab}		Vcab	20	
	19	<u>AI1 ch22</u>		V_{cab}		GND_A	19	
	35	AI1 ch23		I_{ga}		Iga	21	
	2	<u>AI1 ch23</u>		I_{ga}		GND_A	22	
	18	AI1 ch24		I_{gb}		Igb	23	
	34	<u>AI1 ch24</u>		I_{gb}		GND_A	24	
	-	-		I_{gc}		Igc	25	
	-	-		I_{gc}		GND_A	26	

Table 5: ANALOG PINOUT OF dSPACE.

The cables were soldered on a DS50 connector on the dSPACE side and crimped to a J26 connector on the Guasch board.

The FPGAs of the converters were reprogrammed according to the newly wired pinout.

6.2 Grid Emulator Control

The grid emulator consists of a Full 4-Quadrant Grid Simulator by Regatron, shown in Fig. 40. The emulator is being used as a signal amplifier, this means that the emulator is receiv-

ing an analog three phase voltage signal with an amplitude of 10 V and it is amplifying it to the desired 120 V_{RMS} (line voltage). The emulator is capable of 50 kVA and it is supplied by the grid.

The analogue signals come from the PLEXIM RTBox, shown in Fig. 46, a micro-controller capable of performing a real-time PLECS simulation and to send the analog signals to the emulator. The simulation can generate harmonic perturbations, voltage dips, phase jumps, voltage distortion and, with my contributions, dynamic frequency regulation.



Figure 46: RTBox [33].

6.2.1 Dynamic Frequency Regulation

Using the swing equation introduced in chapter 3.3 it is possible to impose the grid frequency to the emulator, the PLECS simulation receives the current of the grid interface and through the use of power hardware in the loop it determines the grid interface power, as shown in the block diagram in Fig. 47. The frequency is then integrated to obtain the angle of the voltage phasor. One of my contribution in this thesis has been the wiring, testing and installation of the rack current conditioning board and the implementation of the current measures in the real time system.

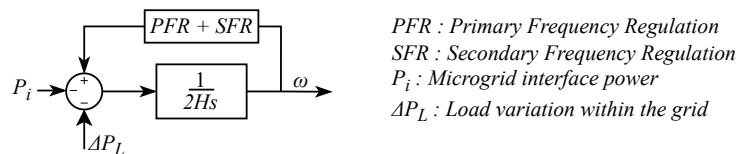


Figure 47: Swing equation using the grid interface feedback power.

The grid model emulates a primary and secondary frequency regulation using a statism of $b_p = 5\%$ and a time constant of the secondary regulation of $T_s = 50$ s. The ΔP_L is used to emulate grid contingencies and it is expressed in p.u. of the grid base power. The interface power P_i is the power calculated using the interface currents with (80)

$$P_i = \frac{v_\alpha^{ref} \cdot i_\alpha^{meas} + v_\beta^{ref} \cdot i_\beta^{meas}}{V_b^{grid} \cdot I_b^{grid}} \quad (80)$$

6.3 Rack Current Conditioning Board

The rack current conditioning board of Fig. 48 is needed to interface the closed loop hall effect sensors to the RTBbox control; its goal is to transform the current output of the sensors into an analog voltage. The board offers the possibility of transmitting the signal both in a differential and unipolar way.

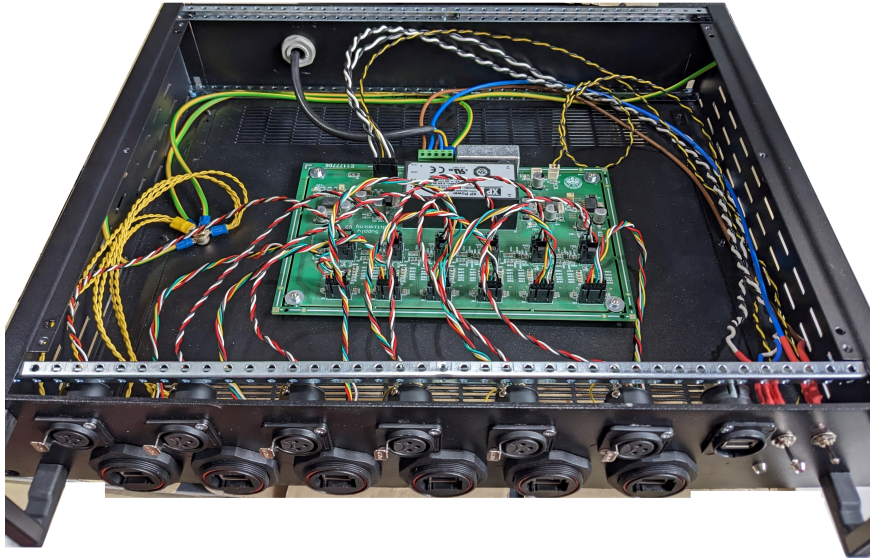


Figure 48: Current acquisition board.

The current sensors are connected to the board via Ethernet cables of Fig. 49; the board allows, through the switch (S2) represented in Fig. 50, to connect the supply ground to the reference ground of the analog sensors. This is to ensure that the common mode currents of the low voltage circuit are connected through a low impedance to the real ground, these currents would otherwise circulate through the distribution lines and connect through an impedance, the voltage drop that would ensue could generate disturbances in the measured voltage.

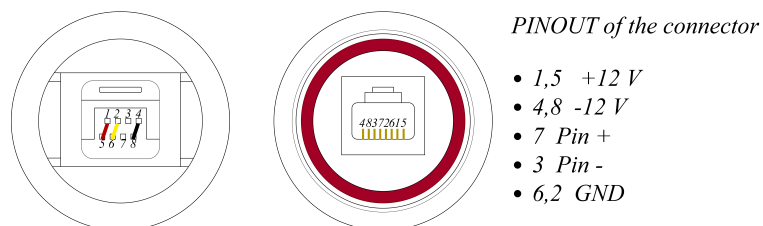


Figure 49: Ethernet connector pinout for the current sensor.

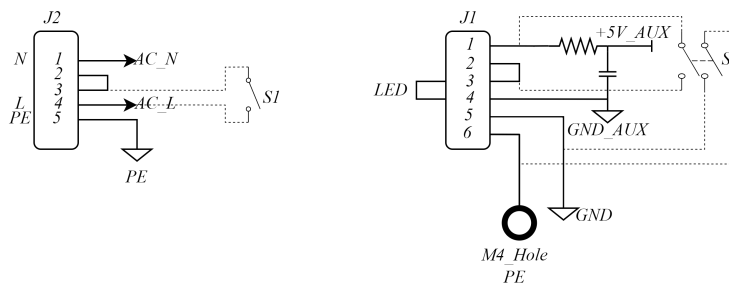


Figure 50: Power connector (J2) and ground switch connector (J1)

The ethernet connector, in Fig. 49, is wired to the J6 connector on the board, Fig. 51. The output pins are J5 for the differential amplifiers and J7 for the unipolar amplifier.

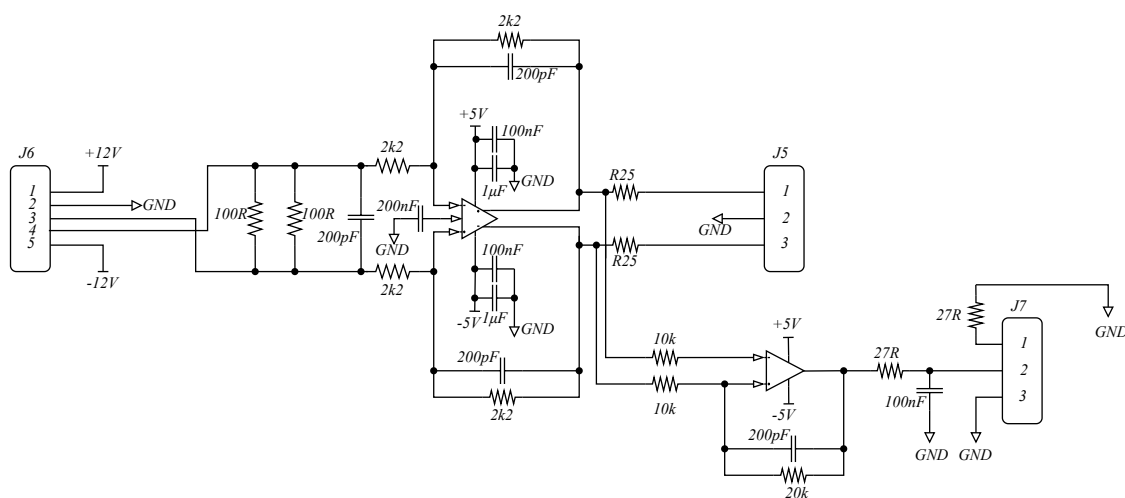


Figure 51: Amplifying circuit for each channel.

The current from the pins 3 and 7, coming from the closed-loop hall effect sensor, flows through the two 100 Ω resistors in parallel and is turned into a voltage. The amplifying ratio of the op-amp is given by the ratio of the input resistance and the transversal resistance; in our case both are equal to 2.2 kΩ, therefore it is equal to 1.

The turn ratio of the hall effect used is 2000, the input resistances are 50 Ω, so the voltage to current gain is:

$$\frac{v_{amp}}{I} = \frac{1}{40} \quad (81)$$

The signal v_{amp} is then fed to the RTBox analog input board and acquired by the simulation in real time.

6.4 Microgrid

The last experimental setup consists in assembling a microgrid with the use of the grid emulator and three inverters. The layout of the microgrid is shown in Fig. 52.

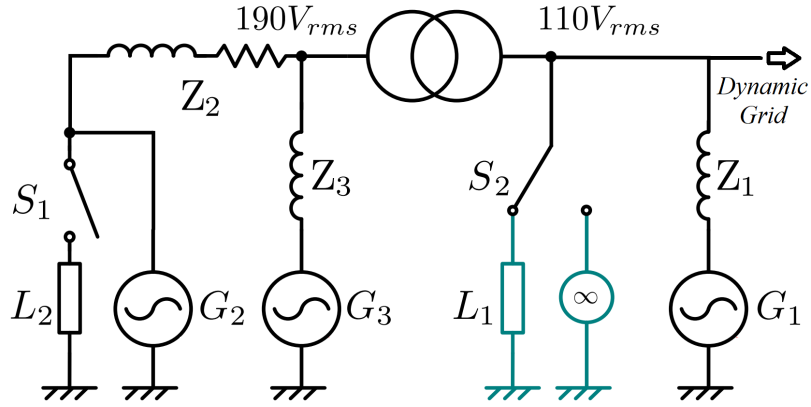


Figure 52: Microgrid layout.

The final laboratory setup is as shown in Fig. 53.

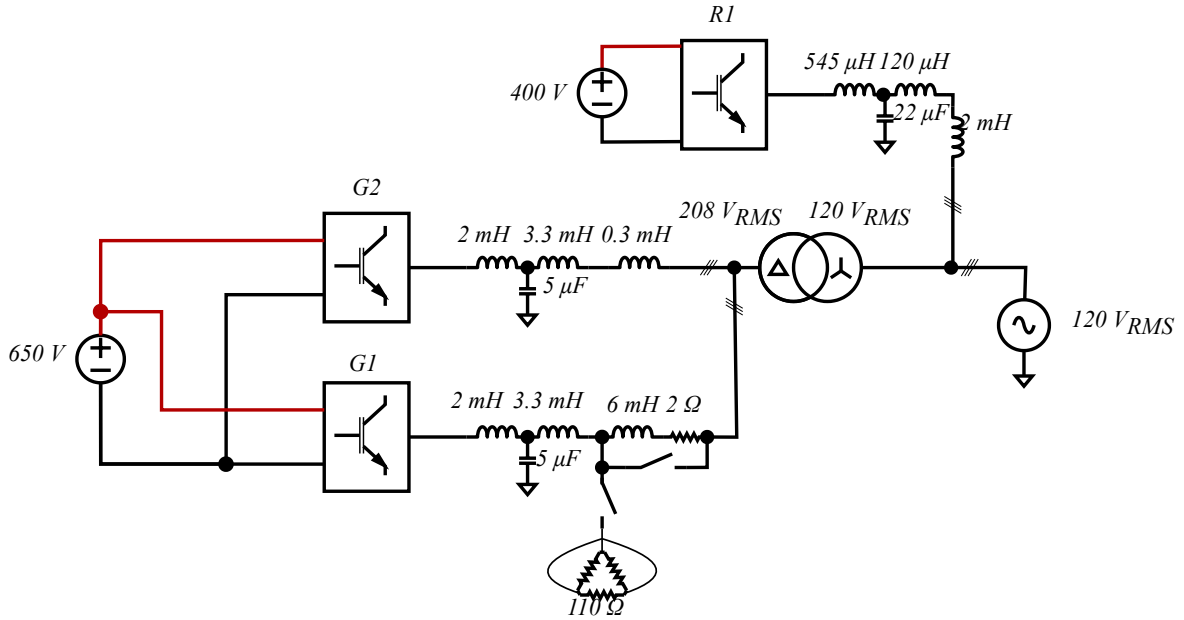


Figure 53: Laboratory microgrid schematic.

It is useful to the analysis to represent the Microgrid of Fig. 53 in p.u.. First it is necessary to calculate the grid p.u. values, done in Table 6

Grid base voltage	V_b	$208 \cdot \sqrt{2} \hat{V}$
Grid base power	S_b	15 kVA
Base current	I_b	34.0 \hat{A}
Base impedance	Z_b	8.65 Ω
Base inductance	L_b	0.0275 H
Base capacitance	C_b	367 μF

Grid base voltage	V_b	$120 \cdot \sqrt{2} \hat{V}$
Grid base power	S_b	15 kVA
Base current	I_b	58.9 \hat{A}
Base impedance	Z_b	2.88 Ω
Base inductance	L_b	0.00917 H
Base capacitance	C_b	1.105 mF

Table 6: BASE VALUES FOR 208 AND 120 V_{RMS} .

The results of the per unit conversion are shown in Fig. 54, they show that R1 has a line impedance greater than 0.2 p.u. – this means a short circuit current less than 5 p.u. – in the same way G1 and G2 see impedances greater than 0.3 and 0.1 respectively.

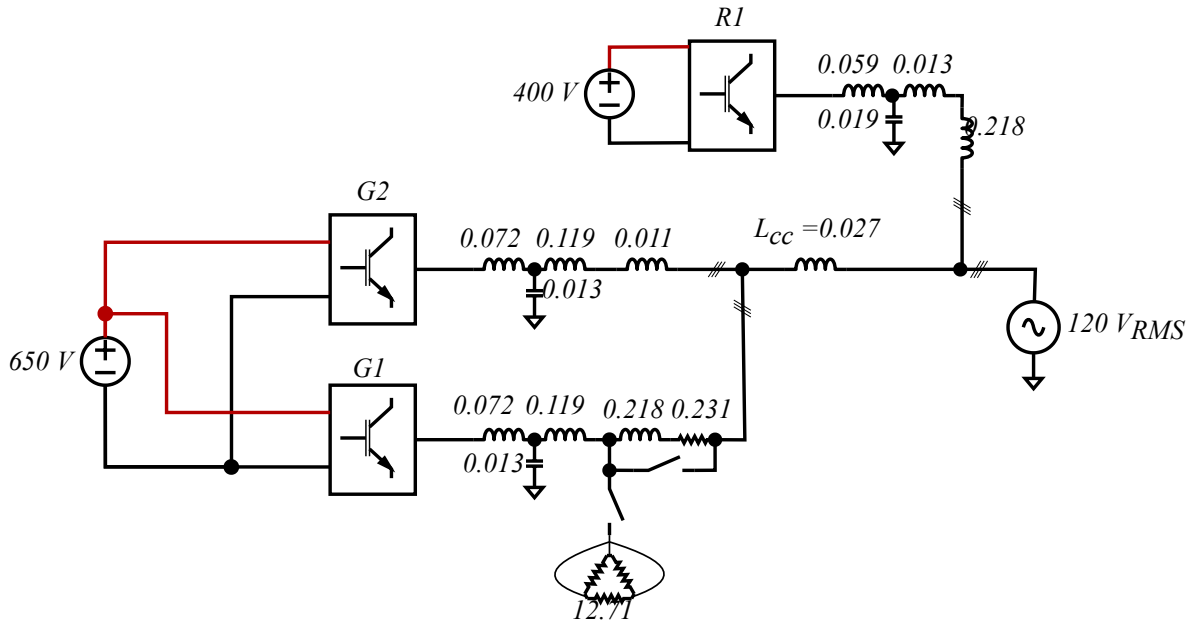


Figure 54: Per unit schematic of the microgrid.

The distribution system is characterized by different short circuit/line impedances depending on the voltage level.

They generally are:

LV Low voltage distribution system generally have the smallest line impedances of all, this is due to the low base power with respect to the MV feeders and the typical transformer impedance of 0.08 p.u., this is because the voltage drop on the line needs to be relatively small due to the absence of compensation.

MV Medium voltage lines have line impedances ranging from 0.15 to 0.2 p.u., the reason is that MV feeders have voltage compensation and the short circuit currents would otherwise be too big to handle.

HV High voltage distribution lines are characterized by the highest short circuit impedances, this is due to their greater length compared to the other voltage levels and the much higher base power, which would result in too high fault currents; typical line impedance are greater than 0.2 p.u..

This means that the system recreated in the laboratory resembles an isolated HV or MV node in a transmission system, this could be associated by a remote renewable energy source linked to the main DG. Even though the voltage levels resemble those of LV distribution systems.

7 Experimental Results

This chapter aims at showing the results obtained in the experimental setup described in 5 and comparing the results to the theory introduced.

7.1 Single Inverter with Variable Grid

The first experiment with the variable grid is carried out using the following parameters:

Grid base power	S_b	15 kVA
Grid time constant	H	4 s
Contingency	ΔP_L	0.1 p.u.
VSM time constant	H	4 s
VSM virtual resistance	R_v	0.02 p.u.
VSM virtual inductance	L_v	0.1 p.u.
VSM excitation time constant	T_e	1 s

Table 7: R1 SIMULATION PARAMETERS.

The experimental results of Fig. 55 show how, after the contingency, the S-VSC injects inertial power into the grid, the inverter power affects the grid power P_{grid} which is the result of the primary and secondary regulation. The inertial power contribution is reflected on the grid's frequency of Fig. 56, decreasing the ROCOF and shifting the Nadir upward and rightward.

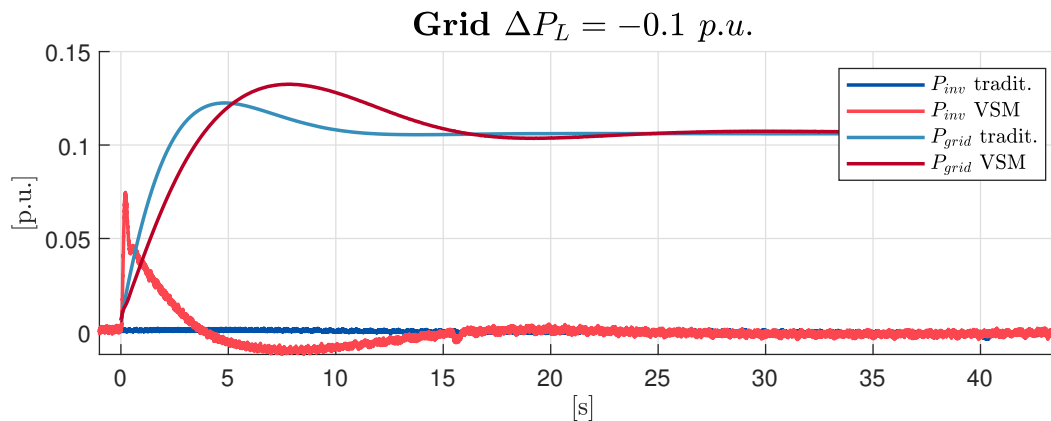


Figure 55: Active power injection response to grid contingency using traditional controls and S-VSC

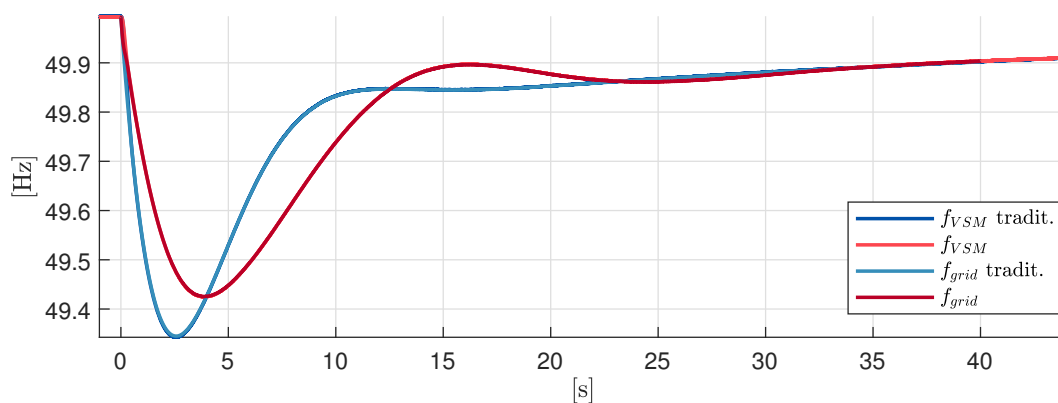


Figure 56: frequency behavior after grid contingency using traditional controls and S-VSC.

Fig. 57 shows the comparison between the experiment carried out in the laboratory and the PLECS simulation used to study the phenomena involved; as the result show, the result are in line with the experiments – which are affected by measurement errors which can be seen in Fig. 57b; the cyan line P_{inv}^{lpf} is the measured power displayed with a low pass filter of 10 Hz.

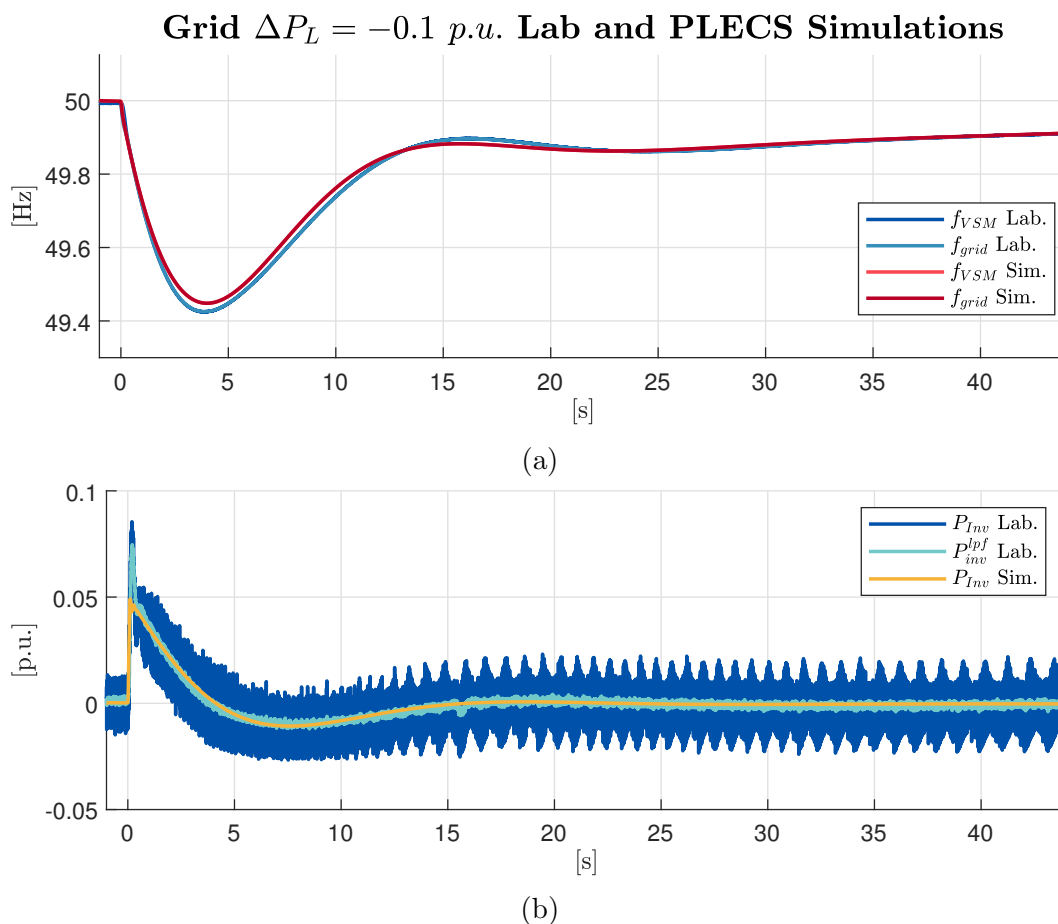


Figure 57: PLECS simulation and experimental result comparison.

The frequency of the center of inertia, defined in (37), is necessary to evaluate the ROCOF properly due to the presence of oscillations in the grid and VSC frequency, shown in Fig. 58b.

Fig. 58a indicates how, thanks to the inertial contributions, the Nadir increases from 49.345 Hz to 49.425 Hz, while calculations of the ROCOF yield:

$$ROCOF_{tradit.} = \frac{\Delta f}{\Delta t} = \frac{49.9311 - 49.9925}{0.1036 - 0.002} = 0.604 \frac{\text{Hz}}{\text{s}} \quad (82)$$

$$ROCOF_{VSM} = \frac{\Delta f}{\Delta t} = \frac{49.93 - 49.9925}{0.1971 - 0.002} = 0.320 \frac{\text{Hz}}{\text{s}} \quad (83)$$

By applying (27) we can calculate the theoretical values for the experiment performed; the TSI of the traditional control is $H_{tradit.} = 4s$ while with the contribution of the VSM it becomes $H_{VSM} = 8s$.

$$ROCOF_{tradit.} = \frac{\Delta P_L}{2H_{tradit.}} \cdot f_{base} = \frac{0.1}{2 \cdot 4} \cdot 50 = 0.625 \frac{\text{Hz}}{\text{s}} \quad (84)$$

$$ROCOF_{VSM} = \frac{\Delta P_L}{2H_{VSM}} \cdot f_{base} = \frac{0.1}{2 \cdot 8} \cdot 50 = 0.3125 \frac{\text{Hz}}{\text{s}} \quad (85)$$

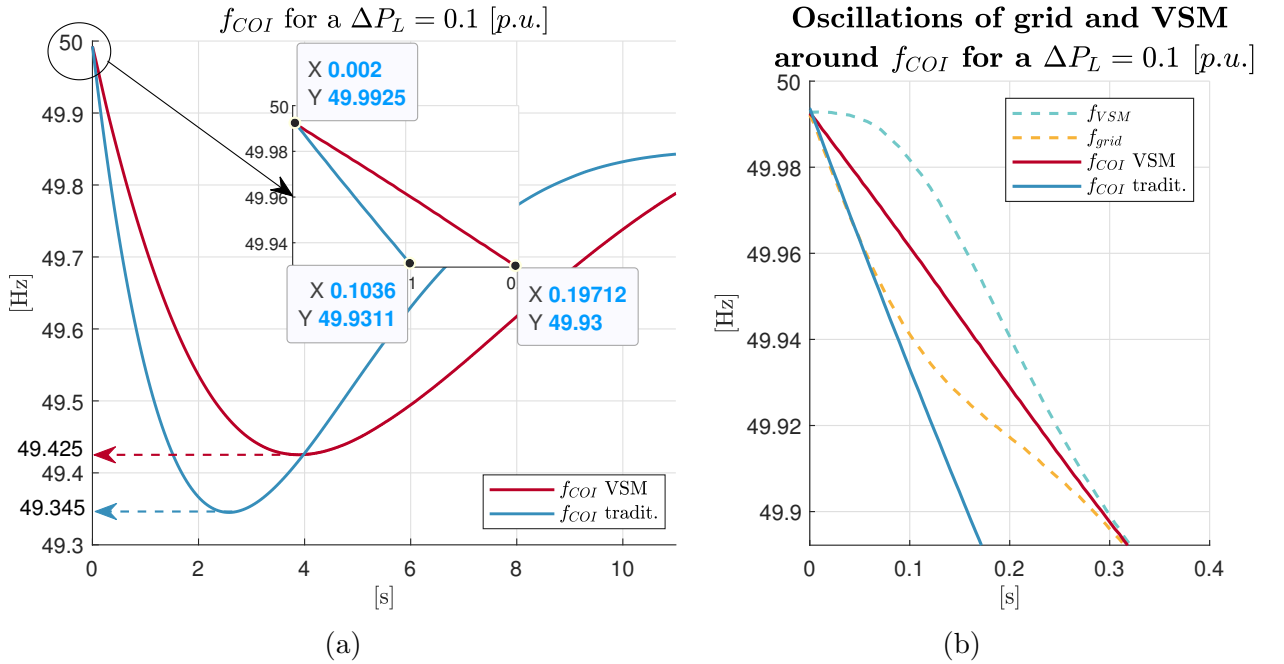


Figure 58: ROCOF, Nadir and oscillations detailed view.

The test was then repeated and shown in Fig. 59 changing the grid's TSI to 10 seconds and were then compared to the ones described above; this is to show the inertial contribution of the VSM to a stiffer grid. The results can be read as a traditional grid with high inertia $H = 10s$ and a renewable based grid, with a lower inertia $H = 4s$ – which could be provided by hydroelectric and hydrogen turbines.

The ROCOFs for each analyzed contingency are reported in Table 8.

Contingency ROCOF for stiff grid	
$ROCOF_{10s \text{ tradit.}}$	0.250 Hz/s
$ROCOF_{10s + VSM}$	0.179 Hz/s
$ROCOF_{4s \text{ tradit.}}$	0.625 Hz/s
$ROCOF_{4s + VSM}$	0.313 Hz/s

Table 8: ROCOF VALUE FOR DIFFERENT TSI.

As the results show, the contribution of the VSM diminishes as the inertia of the grid increases; the contribution to the ROCOF is 0.071 Hz/s for a grid inertia constant (H) of 10 seconds and 0.313 Hz/s for 4 seconds.

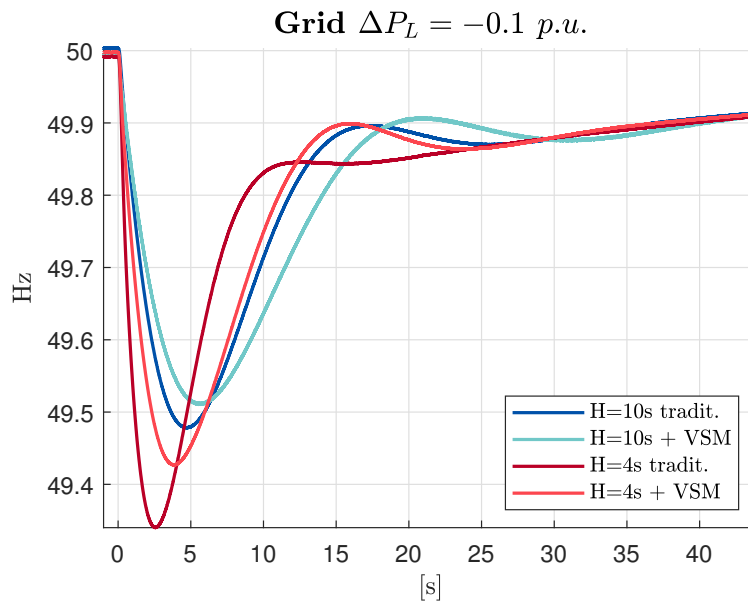
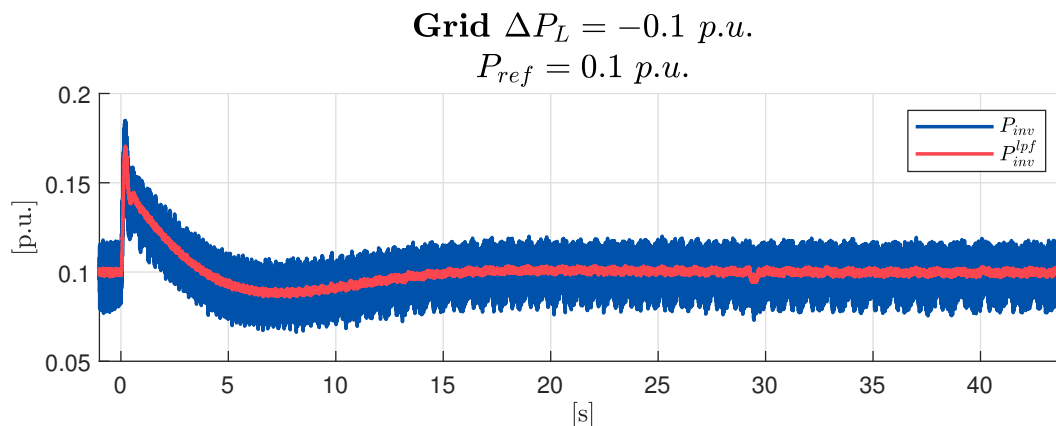


Figure 59: Comparison of contingencies with a stiff grid.

A similar experiment to the one shown in Fig. 57b has been carried out in Fig. 60. in this case the reference power of the inverter has been set to 0.1 p.u.. This represents for example a working PV plant, who reacts to a grid fault. The inertial contribution would need to be fulfilled by an installed energy storage if the PV plant – or any installed energy production plant – is not capable of delivering it.

Figure 60: $P_{ref} = 0.1$ p.u. contingency inertial response.

7.2 Two Inverters with Variable Grid

The setup was then tested with the two Guasch inverters (G1 and G2 in Fig. 61); before performing the tests the two inverters have undergone a period of refurbishment described in Chapter 6.1.

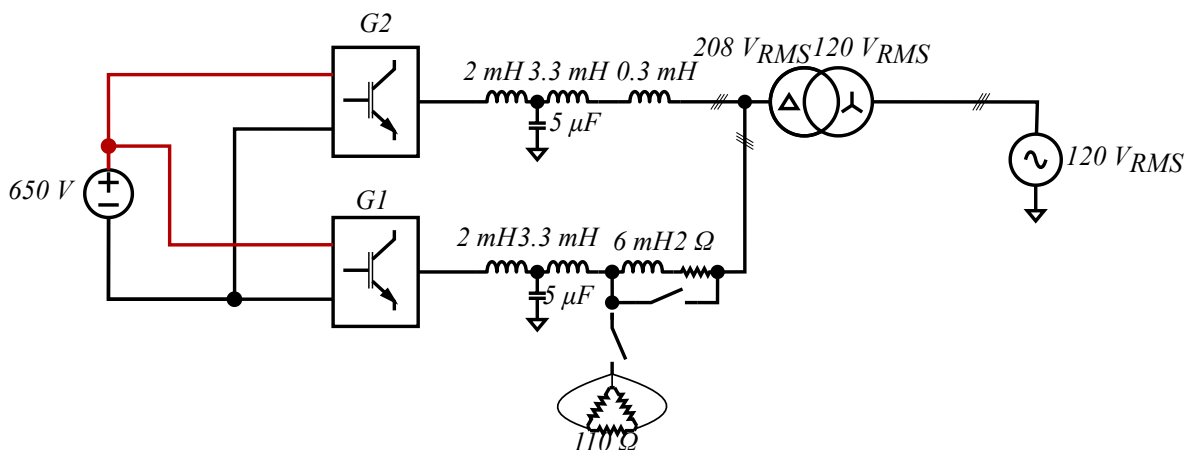


Figure 61: Laboratory microgrid schematic.

The Virtual Machine parameters, for this first test, were kept equal and are reported in Table 9.

Grid base power	S_b	15 kVA
Grid time constant	H	4 s
Contingency	ΔP_L	0.1 [p.u.]
VSM time constant	H	4 s
VSM virtual resistance	R_v	0.02 [p.u.]
VSM virtual inductance	L_v	0.15 [p.u.]
VSM excitation time constant	T_e	1 s

Table 9: G1 & G2 SIMULATION PARAMETERS.

With respect to the experiments of Chapter 7.1 the virtual inductance was increased from 0.1 $p.u.$ to 0.15 $p.u.$, this is due to the tests being performed on a weak grid, described in Chapter 6.4.

Compared to the results shown in Fig. 55, each inverter of Fig. 62a – having the same base power S_b and inertia time constant H of the grid – responds to the 0.1 p.u. fault injecting circa 1/3 of the contingency power (0.033 p.u.), this is due to the sharing of the inertial power being proportional to the aforementioned parameters. The ROCOF is then decreased due to the imbalance acting on each virtual rotor being smaller, this in turns increases the Nadir.

Fig. 63 and Fig. 64 show the two inverters being controlled with traditional and S-VSC controls. As it is clear, the traditional control does not respond to frequency deviations and it thus does not contribute to the inertial response; the other inverter is thus forced to provide a greater share of inertial power – in theory 0.05 p.u. or half of the contingency – and this causes higher values of ROCOF.

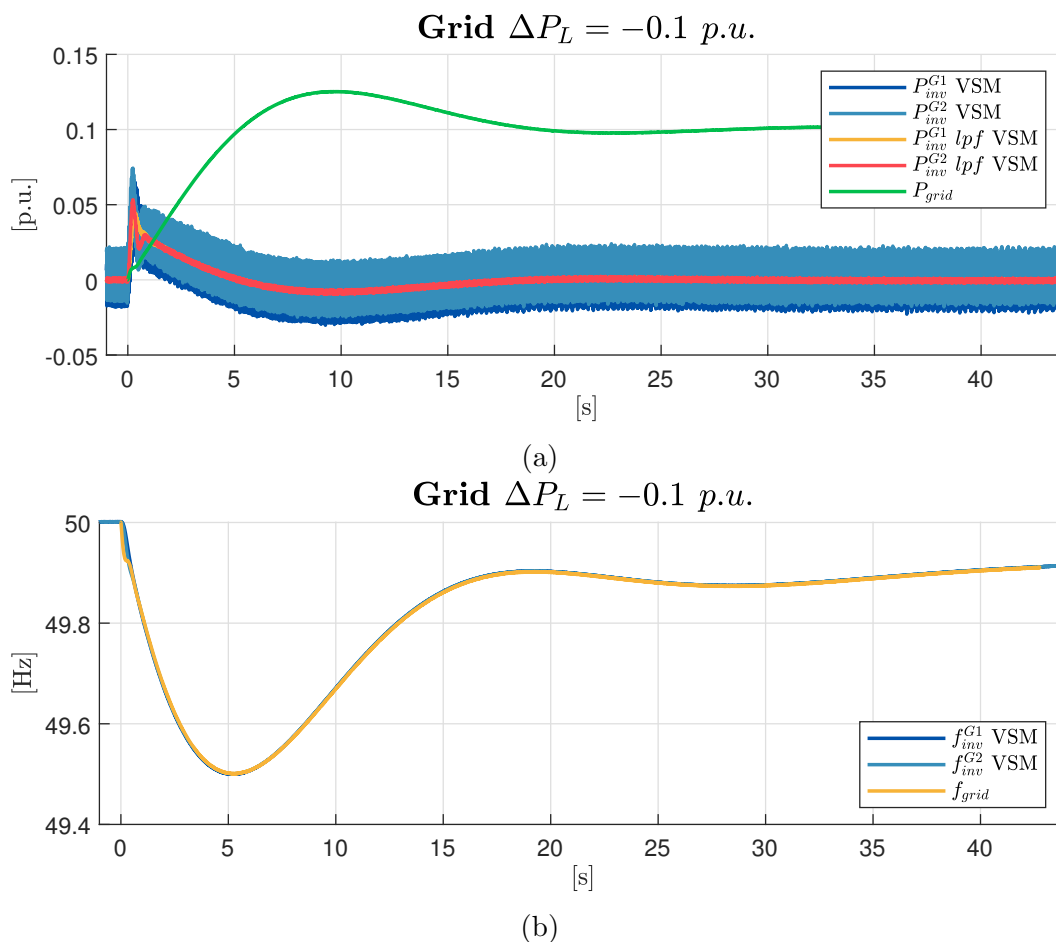


Figure 62: Grid contingency response using S-VSC, two inverters (G1 and G2) connected.

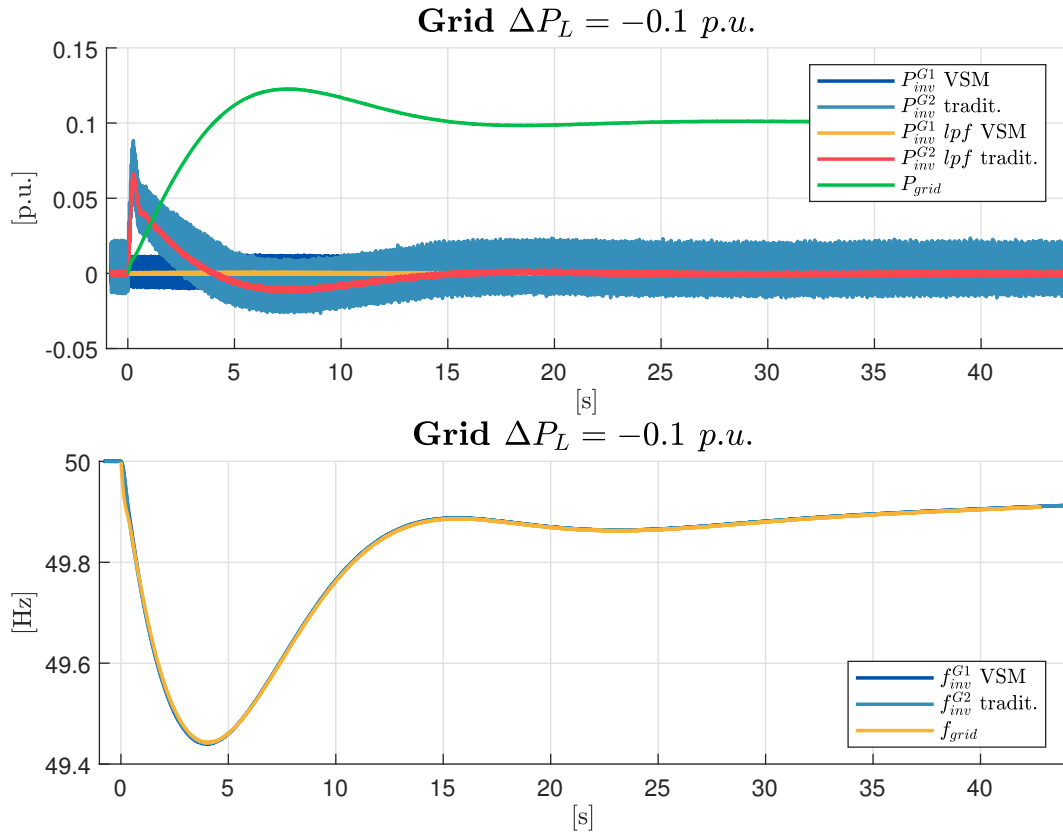


Figure 63: G1 inverter implementing S-VSC, G2 inverter implementing traditional controls.

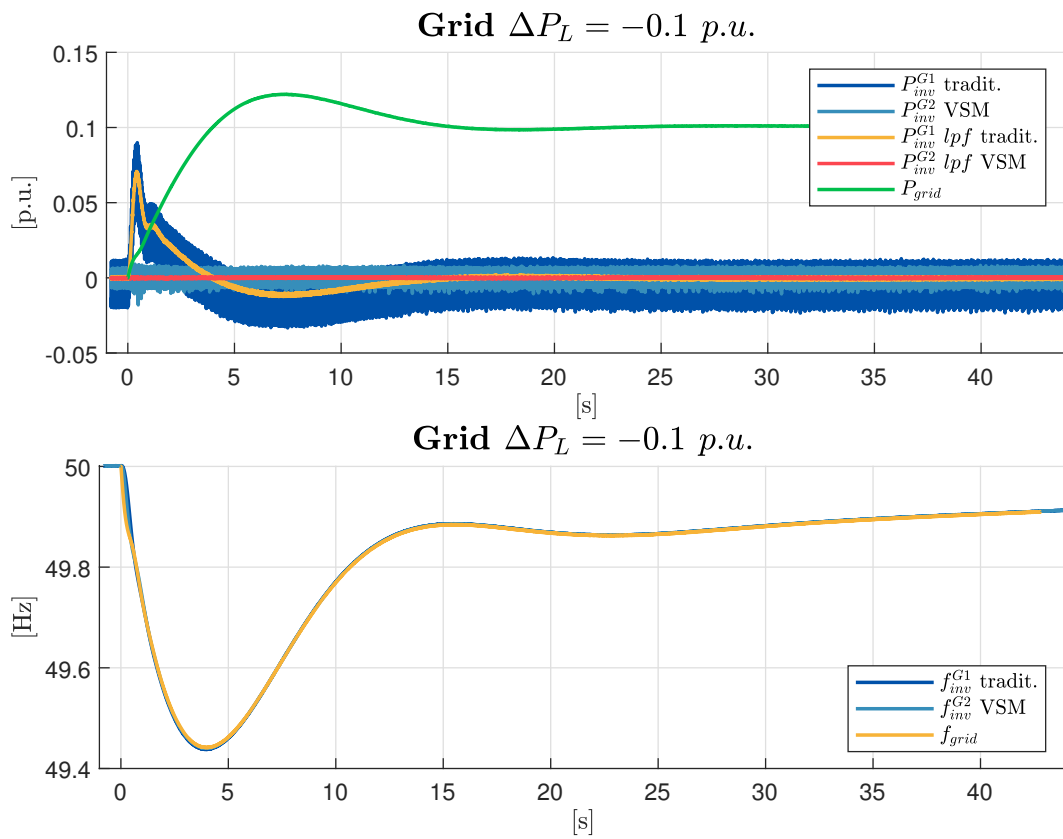


Figure 64: G2 inverter implementing S-VSC, G1 inverter implementing traditional controls.

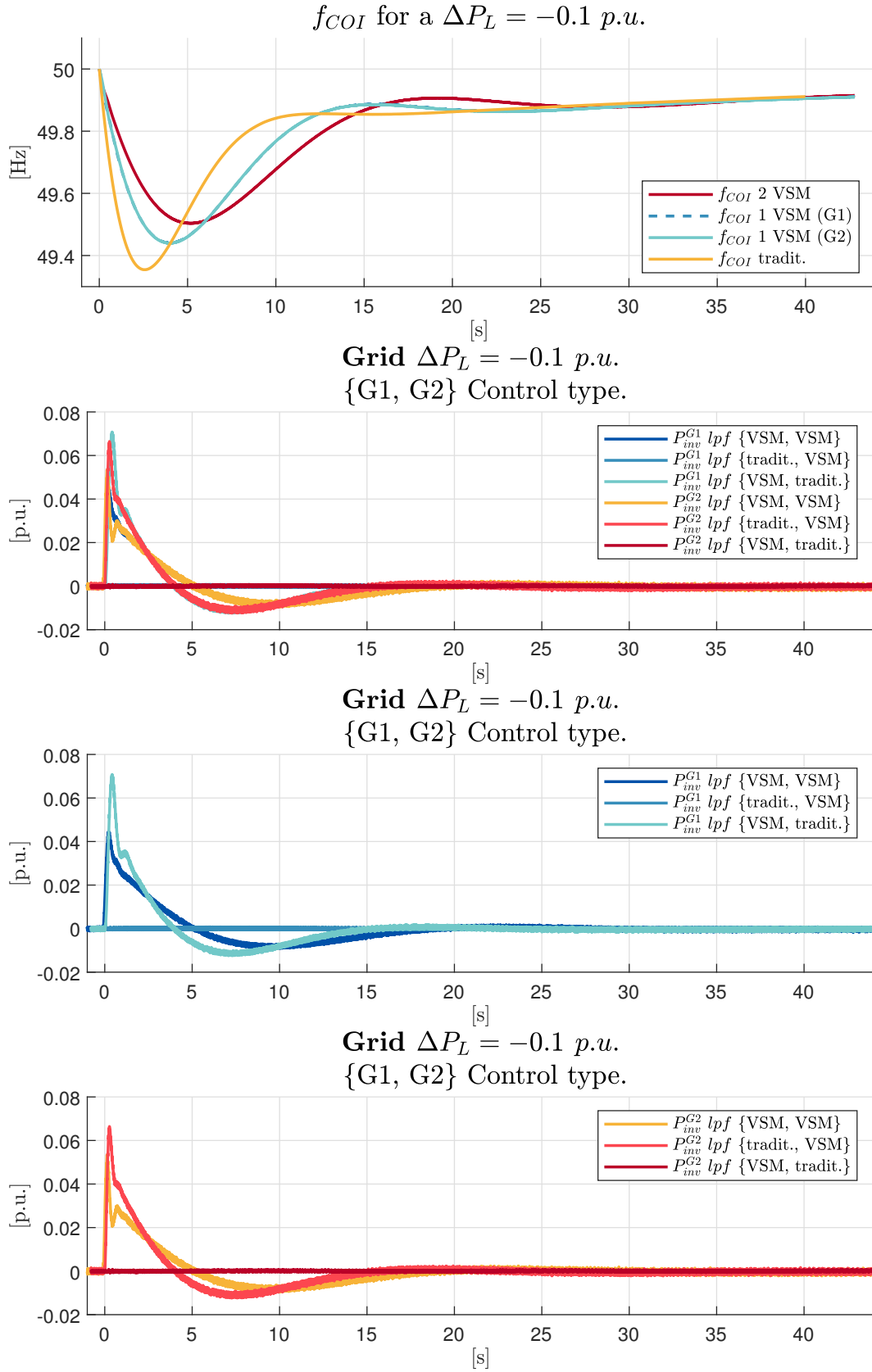


Figure 65: Comparisons of the tests of Fig. 62, 63, 64.

In the Center of Inertia f_{COI} comparison plot of Fig. 65 the result for solely traditional controls was added under " f_{COI} tradit." to show the improvements of the control strategy

for the microgrid under test.

From the comparison of the two S-VSCs we can also conclude that in the time scale $> 1s$ the control strategies are equivalent as mean values; at the instant following the contingency, due to different grid parameters and control loop setup, there is a dynamical difference in the response behavior resulting in under-damped oscillations.

7.3 Three Inverters with Variable Grid

Finally, the tests are performed with the three inverters G1, G2 & R1 connected to the grid emulator, the setup is reported again in Fig. 66 for convenience.

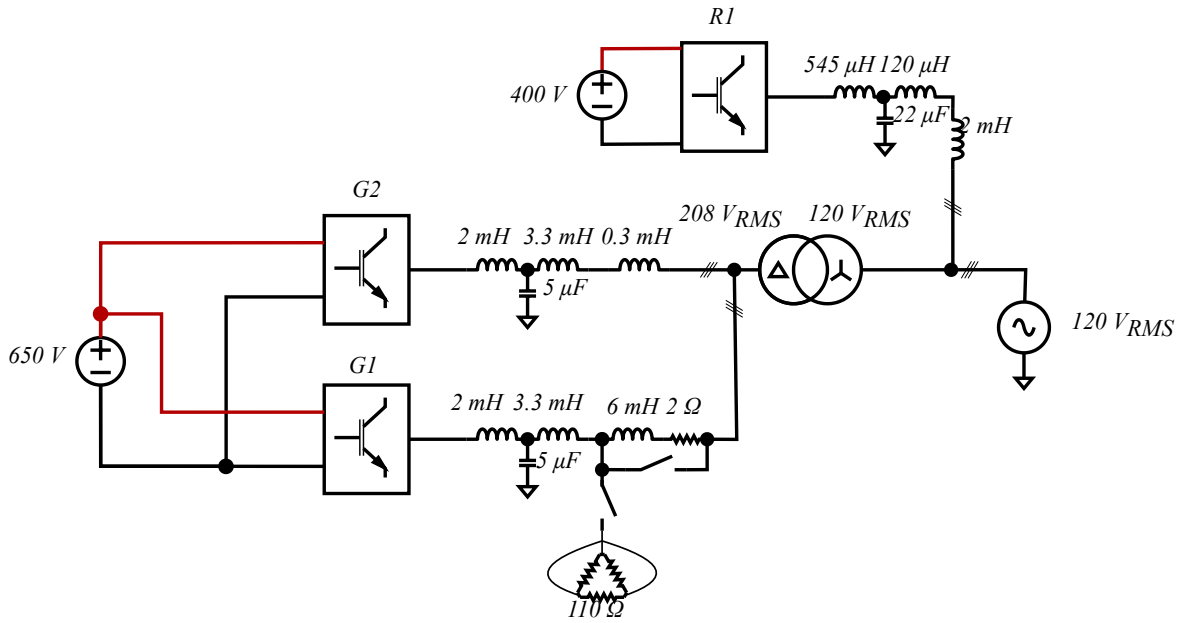


Figure 66: Three inverters with variable grid setup.

The results have been performed with the same values reported in Table 7 and 9 for the R1 and G1 & G2 inverters respectively. According to the inertial power share proportional to the inertia of the generator we can derive the expected peak power of Fig. 67a to be 0.025 p.u.; which, except for the oscillations, is met quite accurately.

The theoretical value of ROCOF of the new microgrid can be calculated by first calculating the TSI (86).

$$H_{microgrid} = H_{grid} + H_{R1} + H_{G1} + H_{G2} = 4 + 4 + 4 + 4 = 16 \text{ s} \quad (86)$$

$$ROCOF = \frac{\Delta P_L}{2H_{microgrid}} \cdot f_{base} = \frac{0.1}{2 \cdot 16} \cdot 50 = 0.156 \frac{Hz}{s} \quad (87)$$

The experimental results yielded a Δf of 0.05 Hz in 0.3375 s, thus

$$ROCOF = \frac{\Delta f}{\Delta t} = \frac{49.95 - 50.00}{0.3375 - 0.0} = 0.148 \frac{Hz}{s} \quad (88)$$

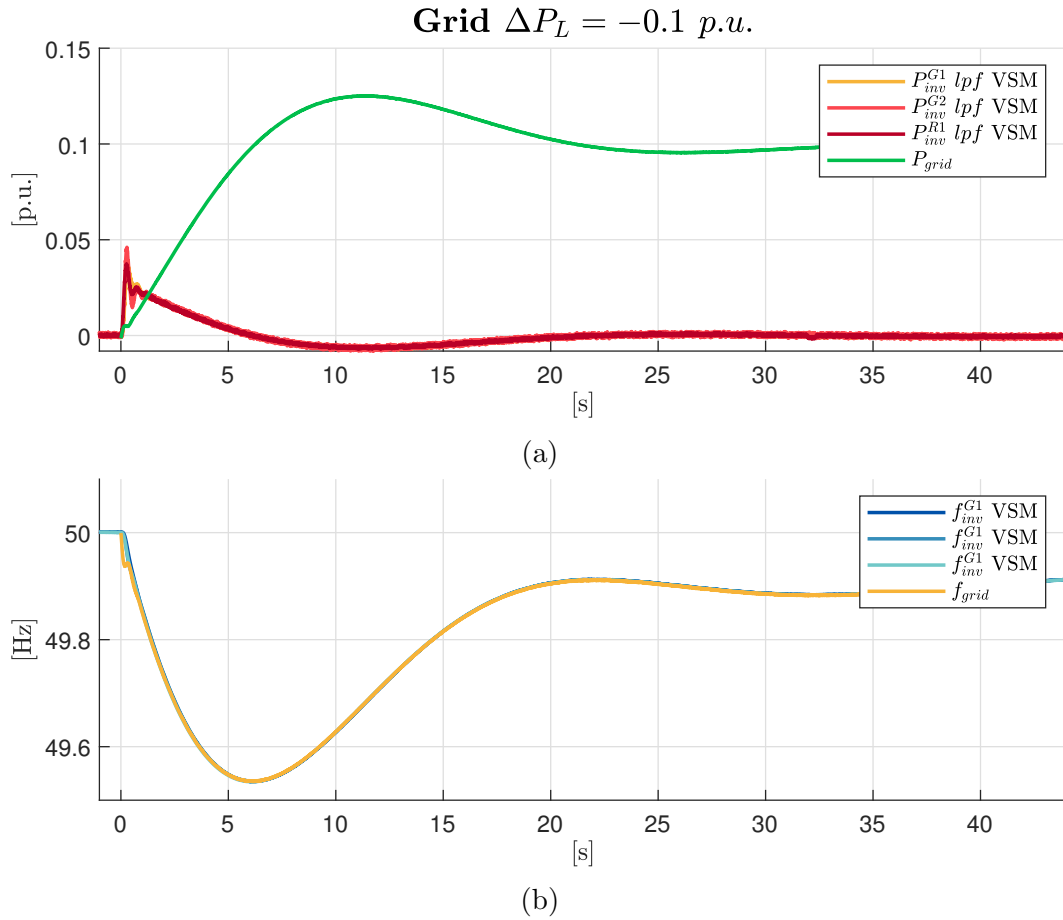


Figure 67: Grid contingency response using S-VSC, three inverters (R1, G1 & G2) connected.

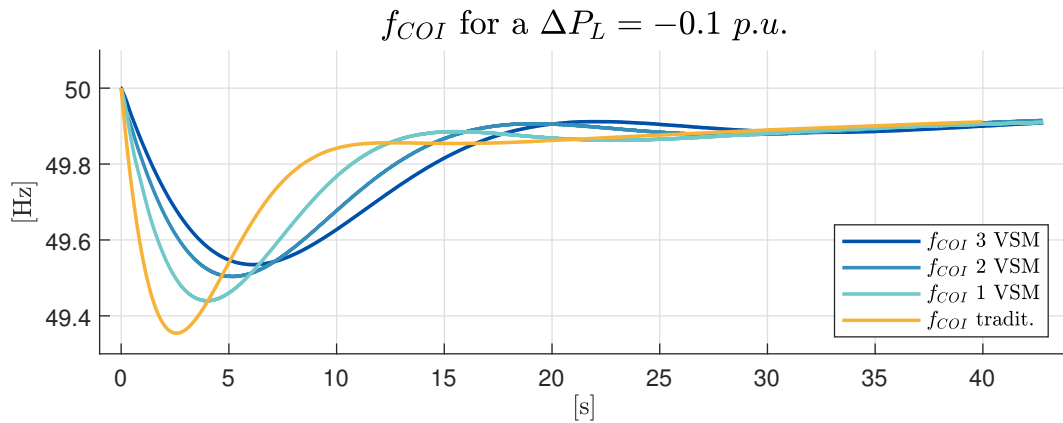


Figure 68: Frequency behavior during grid contingency for different number of VSMs connected.

7.4 Three Inverters with Variable Stiff Grid

To portray a more realistic scenario, the base power of the grid emulator was increased to 100 kVA, this is a relatively low value, but it was chosen to be able to still see the inertial contributions of the different VSMs.

To estimate the power share with the new grid base power it is useful to convert the rotor's time constant H to the inertia M (89).

$$M = \frac{2H \cdot S_n}{f_n} \quad (89)$$

Inertia absolute value M ($H = 4s$)		
Grid	$S_b = 100 \text{ kVA}$	16 kJ/s
R1	$S_b = 15 \text{ kVA}$	2.4 kJ/s
G1	$S_b = 15 \text{ kVA}$	2.4 kJ/s
G2	$S_b = 15 \text{ kVA}$	2.4 kJ/s

Table 10: INERTIA ABSOLUTE VALUE.

Referring to the results of (38), we can conclude that, independently of the base power, the inertial power partitioning is proportional to the inertia M_k ; after having defined $\Delta P_e = \Delta P_L^{pu} \cdot S_b^{grid}$, this yields that the response of each VSM is

$$\Delta P_{e,k} = \frac{M_k}{\sum_i^{N_s} M_k} \cdot \Delta P_e = \frac{2.4}{23.2} \cdot 0.1 \cdot 100 = 1.03 \text{ kW} \quad (90)$$

By transforming the resulting power demand back into the per unit system of the VSM we obtain a predicted inertial response in Fig. 69a of:

$$\Delta P_{e,k}^{pu} = \frac{\Delta P_{e,k}}{S_b} = \frac{1.03}{15} = 0.0689 \text{ p.u.} \quad (91)$$

Generalizing (91) we can derive equation (92) which derives the behavior of a single VSM during a contingency when connected to the grid.

$$\Delta P_e^{pu} = \frac{\Delta P_e}{S_b} = \frac{M}{M + M_{grid}} \cdot \Delta P_L^{pu} \cdot \frac{S_b^{grid}}{S_b} = \frac{2H \cdot S_b}{2H \cdot S_b + 2H_{grid} \cdot S_b^{grid}} \cdot \Delta P_L^{pu} \cdot \frac{S_b^{grid}}{S_b} \quad (92)$$

As the ratio of the grid base power over the VSM base power tends to infinity, as happens for common grid interfaced converters, the per unit response of the VSM is derived in equation (93)

$$\lim_{S_b^{grid} \rightarrow \infty} \Delta P_e^{pu} = \frac{H}{H_{grid}} \cdot \Delta P_L^{pu} \quad (93)$$

This means that the per unit response of the VSM is equal to the per unit value of the contingency of the grid multiplied by the ratio of the inertial constants of the VSM over that of the grid. Therefore we can expect no unforeseen overloads of the converter during ordinary grid contingencies if the inertial constant of the VSM is selected appropriately.

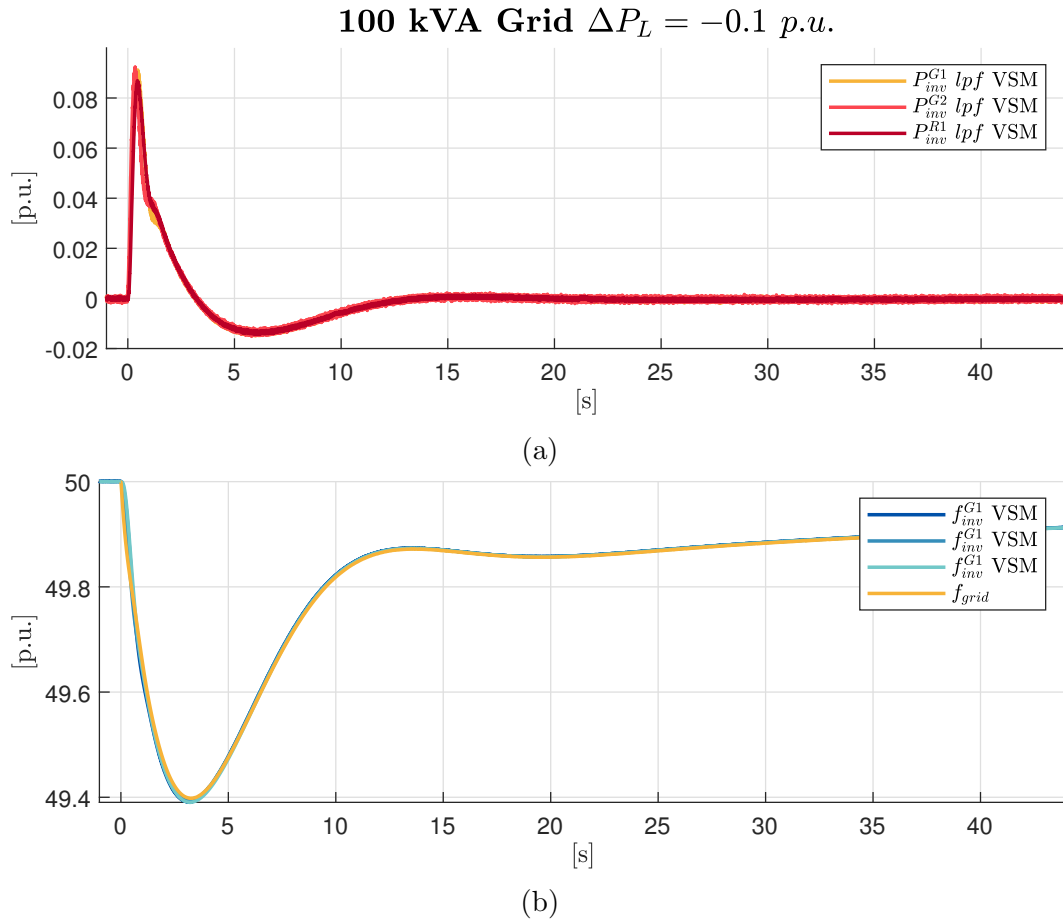


Figure 69: Stiff grid contingency response using S-VSC, three inverters (R1, G1 & G2) connected.

To validate the findings of (92) the tests using a stiff grid were performed changing the converters' inertial constant to 4, 8 and 2 s for G1, G2 and R1 respectively.

The estimation of the inertial response, using (90), is reported in Table 11.

Inertia absolute value M				$\Delta P_{e,k}^{pu}$
Grid	$S_b = 100$ kVA	$H = 4$ s	16 kJ/s	0.0656
R1	$S_b = 15$ kVA	$H = 2$ s	1.2 kJ/s	0.0328
G1	$S_b = 15$ kVA	$H = 4$ s	2.4 kJ/s	0.0656
G2	$S_b = 15$ kVA	$H = 8$ s	4.8 kJ/s	0.1311

Table 11: INERTIA ABSOLUTE VALUE FOR DIFFERENT INERTIAL CONSTANTS.

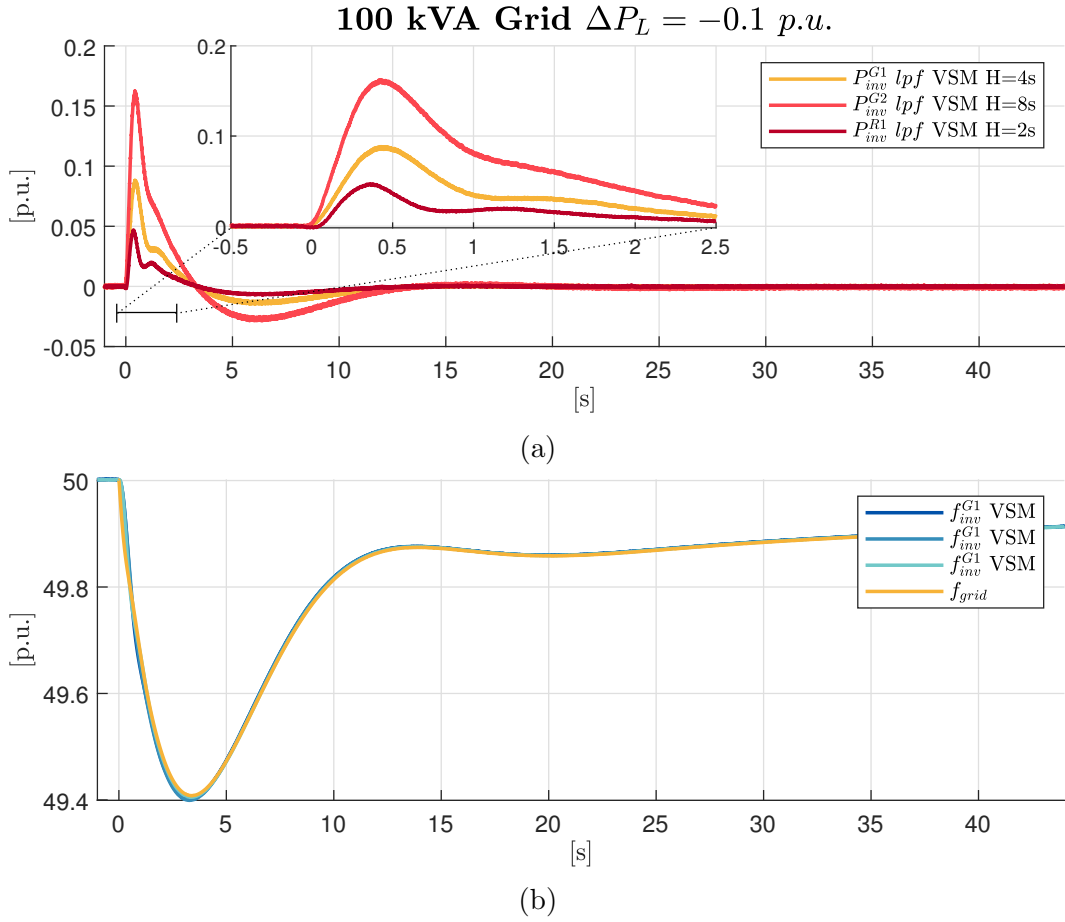


Figure 70: Stiff grid contingency response using S-VSC, three inverters (R1 ($H = 2s$), G1 ($H = 4s$) & G2 ($H = 8s$)) connected.

Using the block diagram of Fig. 57a as reference, the power terms have been displayed in Fig. 71. The term $\sum P_{inv}$ has been obtained by adding the setpoint of the inverters, transforming from the base power of 15 kVA to the grid's one of 100 kVA; this was done to show the accuracy of measurement of the current acquisition board and processing of the variables.

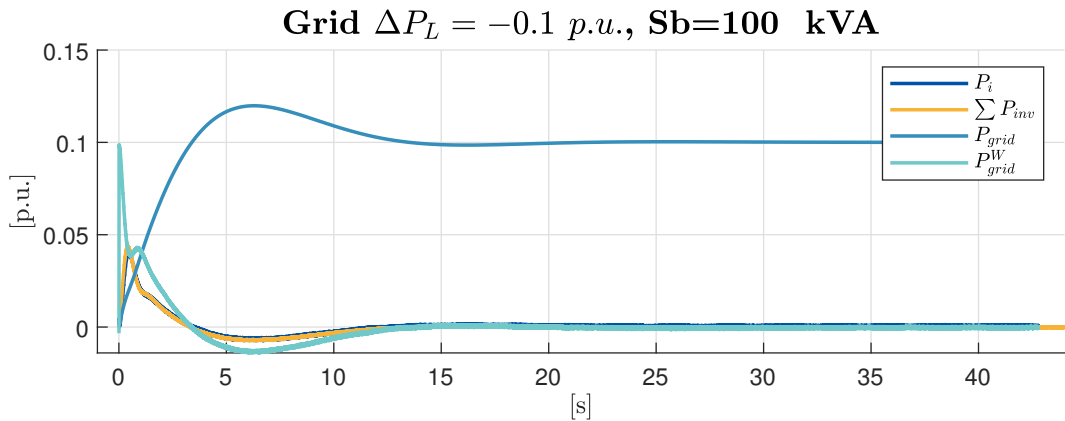


Figure 71: Primary and secondary regulation, microgrid interface and inertial active power terms of the swing equation.

8 Islanding

Islanding refers to a portion of the network – usually a microgrid– separating from the main DG and functioning as an independent grid. The transition can be due to various reasons, the most important being a general blackout or an interruption of service of the DN to which the microgrid is connected.

The islanding maneuver has been simulated in our microgrid. To do this the droop controls of active and reactive power were enabled in the converter G1. Droop controls are equivalent to primary regulation described in chapter 3.3.2. They are characterized by a gain and at steady state they exhibit a error.

The statistics (31) of the droop coefficients selected are:

Active and reactive statistics	
Active statistic	$b_p = 0.02$
Reactive statistic	$b_q = 0.30$

Table 12: DROOP STATISTICS.

The microgrid in the laboratory has been reconfigured as shown in Fig. 72.

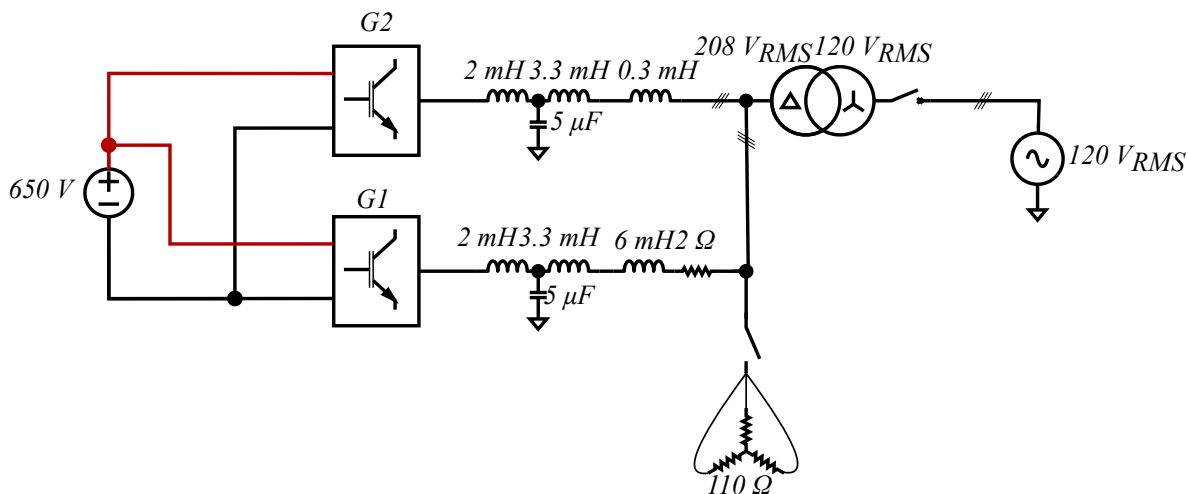


Figure 72: Islanding configuration of the grid.

Fig. 73 shows the frequency behavior of the VSMS, what can be observed is the presence of steady state error. The error is introduced by the proportional gain of the droop controller (30) as it is shown in Fig. 72.

By approximating the voltage to 1 [$p.u.$], the resistive load fed by the microgrid of 12.71 [$p.u.$] draws 0.078 [$p.u.$]. The steady state error can thus be estimated by (94).

$$\Delta f = \Delta P_L \cdot b_p \cdot f_{base} = 0.078 \cdot 0.02 \cdot 50 = 0.078 \text{ Hz} \quad (94)$$

The measured value in Fig. 73 is 0.089 Hz, the small difference can be justified by the presence of additional losses, like commutation losses and the resistive load in the line between G1 and G2.

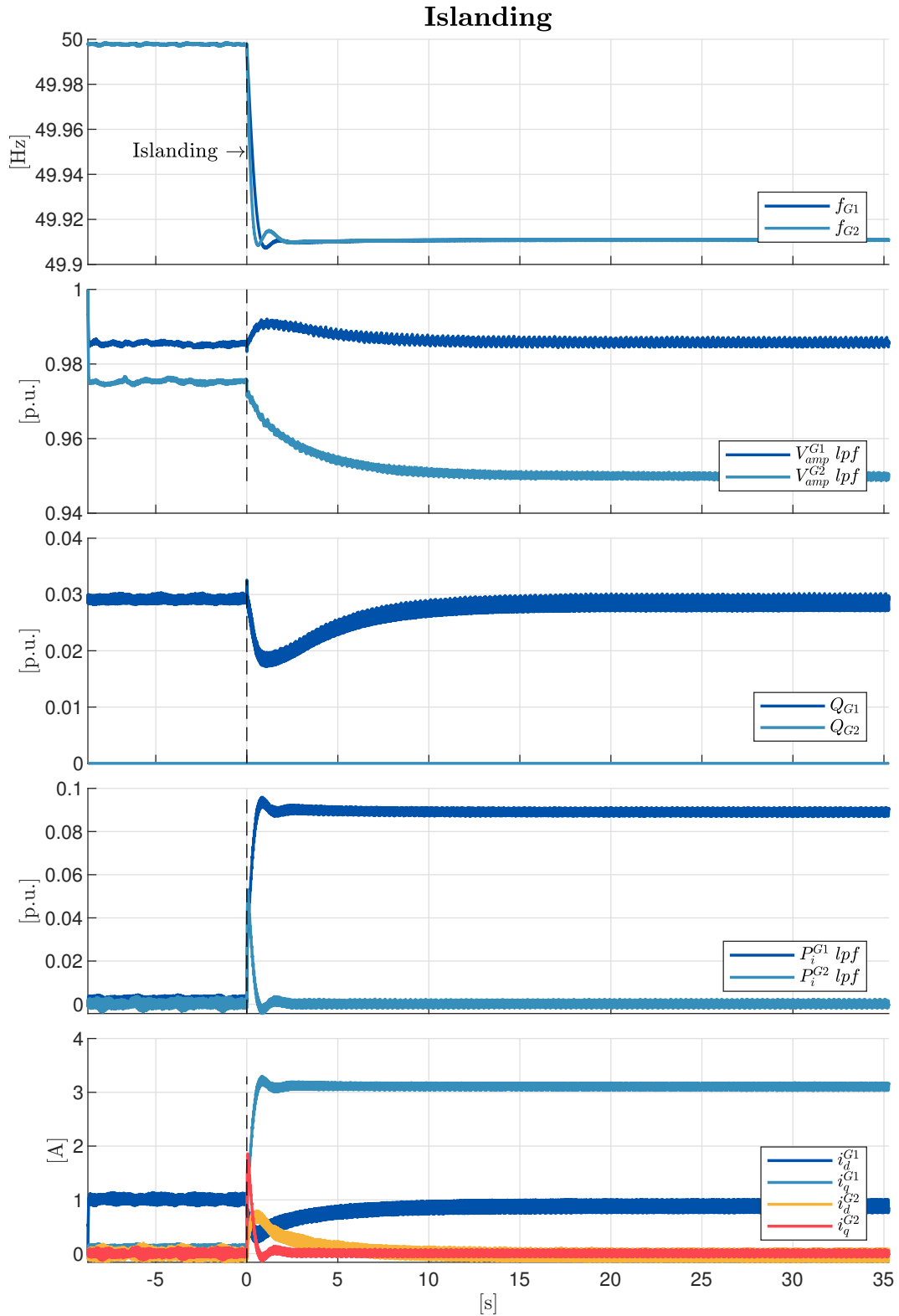


Figure 73: Islanding maneuver results.

9 Conclusions

The thesis has overlooked the implementation of the next generation of grid interfaced static converter controls using VSMS; in particular it focused on the S-VSM and its variations.

The theoretical analysis of chapter 3 has described the fundamentals of power grids, focusing on the services that are carried out by SGs. The ROCOF and related TSI of power grids have been analyzed to show the need for high TSI to ensure the system's stability.

Chapter 4 has analyzed the electro-mechanical model of SGs and how they can be emulated through a simplified electrical circuit; the various damping techniques that are present in literature have also been explained. Damping methods play a crucial role in the inertial response of VSMS, this is why researches are still ongoing. The Lead-Lag damping [32] and RQ damping [28] have been the focus of the lab implementation.

The tests of the control strategy of the static converter has been carried out at PEIC laboratory using the setup introduced in chapter 5. The setup included three inverters and a grid emulator, which I programmed, to simulate the behavior of the grid under normal and contingency operation. The contingencies have been then carried out and the response of the microgrid analyzed in chapter 7.

The results have been performed emulating a load imbalance in the grid and evaluating the inertial contribution. It has been shown how the converters that implement VSM control can and do inject inertial power into the grid. The power injected helps the frequency of the center of mass to undergo a less abrupt change, thus decreasing the value of ROCOF, increasing and delaying the Nadir. By doing that the system is more protected against unnecessary generator disconnection due to too high values of ROCOF or system's underfrequency.

The tests were performed using various VSM constants to evaluate their influence on the control's behavior. All the results were reported and commented alongside the comparison of physical results to the theoretical ones, showing a high level of fidelity.

The final tests were performed in chapter 8 and they consisted in the detachment of the microgrid from the main DG, the control strategies proved resilient enough to keep the microgrid stable even after the detachment.

During the thesis activity the tests performed necessitated works on the setup. In the months spent in the laboratory I:

- Assembled, tested and operated a sensor conditioning board used for the current Hall effect sensors;
- Renewed the digital and analog cabling of the G1 and G2 inverters;
- Modified the existing C-script and interface board of the real time platform dSPACE to control two parallel VSMS;
- Assembled the microgrid connecting the grid emulator (Regatron) and the three inverters (R1, G1 and G2).

9.1 Future Works

The tests to be still performed are numerous, starting from fault tolerance, asymmetrical loads, harmonic contents on the grid, black starts and further testing on islanding capabilities of the S-VSM and its variations.

References

- [1] Gianfranco Chicco and Roberto Napoli. “Challenges for a transition towards the smart grids”. eng. (2018).
- [2] European Commission. “Penetration of renewables and reduction of synchronous inertia in the European power system – Analysis and solutions”. (November 2018).
- [3] Meng Chen, Dao Zhou, and Frede Blaabjerg. “Modelling, Implementation and Assessment of Virtual Synchronous Generator in Power Systems”. *Journal of Modern Power Systems and Clean Energy* (2020).
- [4] Myada Shadoul et al. “A Comprehensive Review on a Virtual-Synchronous Generator: Topologies, Control Orders and Techniques, Energy Storages, and Applications”. *Energies* (2022).
- [5] Politecnico di Torino, Massachusetts Institute of Tehcnology, and Enel. “Electrify Italy”. (2020).
- [6] Gianfranco Chicco and Pierluigi Mancarella. “Distributed multi-generation: A comprehensive view”. eng. *Renewable and Sustainable Energy Reviews* 13.3 (2009), pp. 535–551. ISSN: 1364-0321.
- [7] IPCC. “Special Report on Climate Change and Land - Technical Summary”. (2019).
- [8] COMMISSION REGULATION (EU) 2017/1485. “Establishing a guideline on electricity transmission system operation”. (2 August 2017).
- [9] Deliberation 84/2012/R/EEL. “Urgent actions related ton electricity production systems, with particular reference to the distributed generation, to guarantee the security of the national electrical system”. (8 March 2012).
- [10] Terna. “CENTRALI FOTOVOLTAICHE Condizioni generali di connessione alle reti AT”. (December 2019).
- [11] Pieter Tielens. “Operation and control of power systems with low synchronous inertia”. (November 2017).
- [12] Carpaneto Enrico. “Sistemi Elettrici di Potenza”. (2022).
- [13] European Commission. “Penetration of renewables and reduction of synchronous inertia in the European power system – Analysis and solutions”. (Dec 2020).
- [14] ENTSO-E. “High Penetration of Power Electronic Interfaced Power Sources and the Potential Contribution of Grid Forming Converters”. (2016).
- [15] Terna. “CENTRALI EOLICHE Condizioni generali di connessione alle reti AT”. (December 2019).
- [16] Mandrile Fabio. “Next Generation Inverters Equipped with Virtual Synchronous Compensators for Grid Services and Grid Support”. (January 2021).
- [17] Yong Chen et al. “Comparison of methods for implementing virtual synchronous machine on inverters”. *International conference on renewable energies and power quality*. Vol. 1. 10. 2012.

- [18] Qing-Chang Zhong and George Weiss. “Synchronverters: Inverters That Mimic Synchronous Generators”. eng. *IEEE transactions on industrial electronics (1982)* 58.4 (2011), pp. 1259–1267. ISSN: 0278-0046.
- [19] Qing-Chang Zhong et al. “Self-Synchronized Synchronverters: Inverters Without a Dedicated Synchronization Unit”. eng. *IEEE transactions on power electronics* 29.2 (2014), pp. 617–630. ISSN: 0885-8993.
- [20] K. Sakimoto, Y. Miura, and T. Ise. “Stabilization of a power system with a distributed generator by a Virtual Synchronous Generator function”. eng. *8th International Conference on Power Electronics - ECCE Asia*. IEEE, 2011, pp. 1498–1505. ISBN: 9781612849584.
- [21] “Oscillation Damping of a Distributed Generator Using a Virtual Synchronous Generator”. eng. *IEEE transactions on power delivery* 29.2 (2014), pp. 668–676. ISSN: 0885-8977.
- [22] Yong Chen et al. “Dynamic properties of the virtual synchronous machine (VISMA)”. *Proc. Icrepq* 11 (2011), pp. 755–759.
- [23] Krishnakumar R Vasudevan et al. “Synchronverter: A Comprehensive Review of Modifications, Stability Assessment, Applications and Future Perspectives”. eng. *IEEE access* 8 (2020), pp. 131565–131589. ISSN: 2169-3536.
- [24] Pedro Rodriguez Cortés et al. *Synchronous power controller for a generating system based on static power converters*. US Patent 9,166,508. 2015.
- [25] Yuko Hirase et al. “A grid-connected inverter with virtual synchronous generator model of algebraic type”. *Electrical Engineering in Japan* 184.4 (2013), pp. 10–21.
- [26] M.P.N van Wesenbeeck et al. “Grid tied converter with virtual kinetic storage”. *2009 IEEE Bucharest PowerTech*. 2009, pp. 1–7. DOI: 10.1109/PTC.2009.5282048.
- [27] Salvatore D’Arco, Jon Are Suul, and Olav B. Fosso. “Control system tuning and stability analysis of Virtual Synchronous Machines”. *2013 IEEE Energy Conversion Congress and Exposition*. 2013, pp. 2664–2671. DOI: 10.1109/ECCE.2013.6647045.
- [28] Fabio Mandrile, Enrico Carpaneto, and Radu Bojoi. “Grid-feeding inverter with simplified virtual synchronous compensator providing grid services and grid support”. *IEEE Transactions on Industry Applications* 57.1 (2020), pp. 559–569.
- [29] Xin Meng, Jinjun Liu, and Zeng Liu. “A Generalized Droop Control for Grid-Supporting Inverter Based on Comparison Between Traditional Droop Control and Virtual Synchronous Generator Control”. eng. *IEEE transactions on power electronics* 34.6 (2019), pp. 5416–5438. ISSN: 0885-8993.
- [30] Jia Liu, Yushi Miura, and Toshifumi Ise. “A Novel Oscillation Damping Method of Virtual Synchronous Generator Control Without PLL Using Pole Placement”. *2018 International Power Electronics Conference (IPEC-Niigata 2018 -ECCE Asia)*. 2018, pp. 775–781. DOI: 10.23919/IPEC.2018.8508003.
- [31] Fabio Mandrile, Enrico Carpaneto, and Radu Bojoi. “Virtual Synchronous Generator with Simplified Single-Axis Damper Winding”. *2019 IEEE 28th International Symposium on Industrial Electronics (ISIE)*. 2019, pp. 2123–2128. DOI: 10.1109/ISIE.2019.8781233.

- [32] Fabio Mandrile et al. “A Lead-Lag Filter for Virtual Synchronous Machines with Improved Electromechanical Damping”. *2021 IEEE Energy Conversion Congress and Exposition (ECCE)*. 2021, pp. 583–589. DOI: 10.1109/ECCE47101.2021.9595825.
- [33] Plexim. “RT Box”. (2023). URL: https://www.plexim.com/products/rt_box.

List of Figures

1	Electrify Italy Report [5].	2
2	CO_2 levels and earth temperature recording.	3
3	From Centralized to Distributed Generation. Source: epa.gov.	4
4	Microgrid layout.	5
5	Basic schematic of a distribution system.	6
6	Annex II from Commission Regulation [8].	7
7	Annex III from Commission Regulation [8].	7
8	Fault Ride Through curves for low and medium voltage static converters [10].	8
9	ENTSO-E frequency capability curves for continental Europe [11].	8
10	Sign convention for transmission line analysis.	9
11	Equivalent diagram of the swing equation.	11
12	Time constants for various generation plants. [13]	12
13	Frequency trend during faults.	13
14	System frequency behavior with different TSI.	14
15	Zoomed detail of frequency ROCOF ($\Delta P_L = -0.1$).	14
16	ROCOFs under various TSI.	15
17	Primary regulation control loop.	15
18	Primary regulation control loop with $\Delta f^* = 0$	16
19	Secondary regulation control loop.	16
20	Block diagram of centralized secondary regulation.	17
21	Capability curves of grid interfaced inverters (left) Wind power plants (right) PV powerplants[10, 15].	19
22	V/Q curve (left) Photovoltaic plants (right) Wind farms [10, 15].	19
23	Synchronous generator schematic.	21
24	Three and two phase systems.	21
25	Electrical schematic of the generator's dq axes.	23
26	Electrical schematic of the dq axes.	23
27	Circuitual representation of a steady state synchronous generator.	24
28	Grid interfaced inverter schematic [16].	25
29	S-VSC control schematic.	26
30	Simplified swing equation of the VSM [16].	28
31	Equivalent circuits in the dq axes. (left) d -axis (right) q -axis [16].	28
32	Excitation control block [16].	29
33	Transfer function block and pole representation of the undamped system. .	30
34	Droop control block diagram [16].	31
35	PLL control block diagram [16].	31
36	PI control block diagram [16].	31
37	dq axes winding schematic.	32
38	RQ control block diagram [16].	32
39	LL control block diagram [16].	32
40	Laboratory control desk.	33
41	Electrical schematic of the grid interfaced R1 inverter.	34
42	(left) R1 Inverter interface to dSPACE control unit (right) inverter LCL filter.	34
43	Electrical schematic of the grid interfaced G1 and G2 inverters.	35

44	(left) G1 and G2 Inverter interface to dSPACE control unit (right) inverter LCL filter.	35
45	(left) Transformer (right) grid emulator.	36
46	RTBox [33].	39
47	Swing equation using the grid interface feedback power.	39
48	Current acquisition board.	40
49	Ethernet connector pinout for the current sensor.	40
50	Power connector (J2) and ground switch connector (J1)	41
51	Amplifying circuit for each channel.	41
52	Microgrid layout.	42
53	Laboratory microgrid schematic.	42
54	Per unit schematic of the microgrid.	43
55	Active power injection response to grid contingency using traditional controls and S-VSC	44
56	frequency behavior after grid contingency using traditional controls and S-VSC.	45
57	PLECS simulation and experimental result comparison.	45
58	ROCOF, Nadir and oscillations detailed view.	46
59	Comparison of contingencies with a stiff grid.	47
60	$P_{ref} = 0.1 p.u.$ contingency inertial response.	48
61	Laboratory microgrid schematic.	48
62	Grid contingency response using S-VSC, two inverters (G1 and G2) connected.	49
63	G1 inverter implementing S-VSC, G2 inverter implementing traditional controls.	50
64	G2 inverter implementing S-VSC, G1 inverter implementing traditional controls.	50
65	Comparisons of the tests of Fig. 62, 63, 64.	51
66	Three inverters with variable grid setup.	52
67	Grid contingency response using S-VSC, three inverters (R1, G1 & G2) connected.	53
68	Frequency behavior during grid contingency for different number of VSMS connected.	53
69	Stiff grid contingency response using S-VSC, three inverters (R1, G1 & G2) connected.	55
70	Stiff grid contingency response using S-VSC, three inverters (R1 ($H = 2s$), G1 ($H = 4s$) & G2 ($H = 8s$)) connected.	56
71	Primary and secondary regulation, microgrid interface and inertial active power terms of the swing equation.	56
72	Islanding configuration of the grid.	57
73	Islanding maneuver results.	58

List of Tables

1	UNIT LENGTH PARAMETERS OF A TYPICAL AERIAL TRANSMISSION LINE.	9
2	PARAMETERS OF THE SWING EQUATION.	11
3	CONTROL SCHEME OF THE S-VSM.	26
4	DIGITAL PINOUT OF dSPACE.	37
5	ANALOG PINOUT OF dSPACE.	38

6	BASE VALUES FOR 208 AND 120 V_{RMS}	42
7	R1 SIMULATION PARAMETERS.	44
8	ROCOF VALUE FOR DIFFERENT TSI.	47
9	G1 & G2 SIMULATION PARAMETERS.	48
10	INERTIA ABSOLUTE VALUE.	54
11	INERTIA ABSOLUTE VALUE FOR DIFFERENT INERTIAL CONSTANTS.	55
12	DROOP STATISMS.	57

List of Abbreviations

SG	<i>Synchronous Generator</i>
RES	<i>Renewable Energy Sources</i>
VSM	<i>Virtual Synchronous Machine</i>
V2G	<i>Vehicle to Grid</i>
HV	<i>High Voltage</i>
IED	<i>Intelligent Electronic Device</i>
PMU	<i>Phasor Measurement Unit</i>
SCADA	<i>Supervisory Control and Data Acquisition</i>
DN	<i>Distribution Network</i>
DER	<i>Distributed Energy Resources</i>
PV	<i>Photovoltaic</i>
DG	<i>Distribution Grid</i>
TSO	<i>Transmission System Operator</i>
PFC	<i>Power Factor Correctors</i>
FRT	<i>Fault Ride Through</i>
ROCOF	<i>Rate of Change of Frequency</i>
TSI	<i>Total System Inertia</i>
AVR	<i>Automatic Voltage Regulator</i>
EMF	<i>Electromotive Force</i>
S-VSC	<i>Simplified - Virtual Synchronous Compensator</i>
S-VSM	<i>Simplified - Virtual Synchronous Generator</i>
VSI	<i>Voltage Source Inverter</i>
PLL	<i>Phase Locked Loop</i>
PCC	<i>Point of Common Coupling</i>